

# Electron affinity difference distributions guide the discovery of the superconductor PtPb<sub>3</sub>Bi

Omri Lesser,<sup>1,\*</sup> Yanjun Liu,<sup>1,\*</sup> Natalie Maus,<sup>2,\*</sup> Aaditya Panigrahi,<sup>1,\*</sup> Krishnanand Mallayya,<sup>1</sup> Albert Gong,<sup>3</sup> Anmol Kabra,<sup>3</sup> Scott B. Lee,<sup>4</sup> Sudipta Chatterjee,<sup>4</sup> Amira Merino,<sup>4,5</sup> Kilian Q. Weinberger,<sup>3</sup> Leslie M. Schoop,<sup>4</sup> Jacob R. Gardner,<sup>2</sup> and Eun-Ah Kim<sup>1,6</sup>

<sup>1</sup>*Department of Physics, Cornell University, Ithaca, NY 14853, USA*

<sup>2</sup>*Computer and Information Science Department, University of Pennsylvania, Philadelphia, PA 19104, USA*

<sup>3</sup>*Department of Computer Science, Cornell University, Ithaca, New York 14853, USA*

<sup>4</sup>*Department of Chemistry, Princeton University, Princeton, New Jersey 08544, United States*

<sup>5</sup>*Department of Chemistry, Mercer County Community College, West Windsor, New Jersey 08550, United States*

<sup>6</sup>*Department of Physics, Ewha Womans University, Seoul, South Korea*

Predicting the superconducting transition temperature ( $T_c$ ) from crystal structure and composition remains a central challenge in condensed-matter physics, reflecting the absence of a broadly predictive framework connecting microscopic bonding to macroscopic quantum behavior. Here, we introduce a structure- and chemistry-aware approach implemented in an interpretable Gaussian process model, which we call GP- $T_c$  (Gaussian Process  $T_c$ ), that enables uncertainty-quantified prediction of superconductivity from experimentally accessible inputs. By encoding local bonding environments and geometry as graphlet histograms and learning within a probabilistic framework, we find that the predictive space collapses to a compact set of descriptors: the distribution of electron-affinity differences between neighboring atoms, together with simple elemental features and interatomic distances, provides an informative basis for predicting  $T_c$  across disparate superconducting families. This result identifies an overlooked chemical control parameter while emphasizing the essential role of local structure beyond composition-only approaches. We demonstrate the framework through two complementary tests: validation against a recently established superconducting family and discovery of a previously unknown material. GP- $T_c$  reproduces the experimentally reported  $T_c$  range of the infinite-layer nickelate Nd<sub>0.8</sub>Sr<sub>0.2</sub>NiO<sub>2</sub>. We further predict superconductivity in stoichiometric PtPb<sub>3</sub>Bi and experimentally confirm it through synthesis and bulk measurements, establishing PtPb<sub>3</sub>Bi as a new superconductor with  $T_c \approx 3$  K. To facilitate broad community use, GP- $T_c$  is made available through a web interface for crystal-structure-based prediction, and the same framework identifies additional high-priority superconducting candidates—including SrNiO<sub>2</sub>, K(PRh)<sub>2</sub>, and Ho<sub>2</sub>C<sub>3</sub>—that provide concrete targets for ongoing and future experimental exploration.

Superconductors exhibit macroscopic quantum coherence with vanishing electrical resistance, enabling transformative technologies ranging from high-field magnets and power transmission to quantum information platforms. Despite more than a century of research, predicting the superconducting transition temperature  $T_c$  from a material's crystal structure and composition remains a central unsolved problem in condensed-matter physics. Known superconductors span chemically and structurally diverse families with widely varying  $T_c$ , and no general framework reliably links microscopic bonding and structure to macroscopic superconducting behavior.

Microscopic theories such as Bardeen–Cooper–Schrieffer (BCS) theory and its Eliashberg extension [1] provide a quantitative description of phonon-mediated superconductivity when detailed material-specific inputs are available. In practice, however, these inputs are often difficult to compute or measure accurately, and predictive power deteriorates outside narrowly defined regimes. For unconventional superconductors, a broadly predictive microscopic theory remains elusive. As a

result, superconductivity discovery has relied heavily on empirical heuristics [2], chemical intuition, and serendipity, underscoring the need for complementary approaches that can extract predictive structure–property relationships directly from experimental knowledge.

To transcend human-scale heuristics, data-driven approaches have increasingly sought to learn  $T_c$  directly from known examples. However, the first wave of machine-learning (ML) studies was fundamentally limited by the absence of structural information [3]. Relying solely on chemical formulas, deep neural networks and random forests were used to learn broad statistical trends [4–9] but saw limits without structural information. Although more recent Graph Neural Networks [10, 11] leverage structural information, their implicit incorporation of this information obscures physical insight. Moreover, their focus on Eliashberg theory [12] is only suitable for phononic mechanisms. The challenge, therefore, is to develop a framework that is both *structure-aware* and *interpretable*—one that can capture the holistic nature of bonding and geometry without being constrained by theoretical priors.

Here we argue that progress requires combining structure-aware representations with interpretable learn-

\* These authors contributed equally to the work.

ing to uncover compact, physically meaningful descriptors of superconductivity. Rather than pursuing maximal predictive accuracy through increasingly complex models, we seek organizing principles that transparently link local bonding geometry, elemental chemistry, and superconducting behavior in a way that is predictive, insightful, and experimentally actionable. To this end, we introduce a structure- and chemistry-aware framework that encodes local bonding environments as graphlet histograms derived from experimentally measured crystal structures, taken from the Inorganic Crystal Structure Database (ICSD), and learns their relationship to superconductivity using an interpretable Gaussian-process model we call GP- $T_c$  (see Fig. 1). This approach enables uncertainty-quantified prediction of  $T_c$  while retaining direct access to the features that drive model behavior, allowing systematic identification of the chemical and structural factors most relevant for superconductivity.

Importantly, this perspective does not replace microscopic theory but instead provides a complementary route for identifying promising materials and organizing descriptors that can guide both experiment and subsequent first-principles analysis. Applying this framework reveals a striking compression of the predictive feature space: the distribution of electron-affinity differences between neighboring atoms, together with a small number of elemental and structural descriptors, emerges as a central organizing basis for superconductivity across disparate materials families. This insight enables both family-level understanding and experimentally actionable materials discovery, culminating in the prediction and experimental confirmation of a previously unknown stoichiometric superconductor and the identification of multiple high-priority candidates for future exploration [see Fig. 1(d)].

A central challenge in predicting superconductivity from crystal structure and composition is constructing a representation that is both physically meaningful and amenable to systematic learning. We address this through *graphlet histograms*—a systematic featurization that encodes bonding motifs at multiple scales [Fig. 2(a)]. Graphlets describe atomic neighborhoods hierarchically: first-order graphlets characterize individual atoms through 10 elemental properties (Table S1); second-order graphlets encode neighboring atom pairs through interatomic distances and elemental means and differences (21 features); third-order graphlets extend to atomic triplets, incorporating bond angles (36 features). In total, 67 histogram features per material encode local chemistry and geometry [Fig. 1(b)] in an architecture-independent manner, enabling interpretability unlike graph neural networks that embed structural information implicitly [10, 14].

The distributional features are compared using the Earth Mover’s Distance (EMD) [15, 16], which quantifies the minimal cost to transform one histogram into another and serves as the foundation for constructing a valid Mercer kernel for Gaussian process learning (see

Methods). To capture global symmetry, we construct an 11-dimensional vector by averaging site-specific crystallographic point-group operations over the unit cell (SM Sec. I). Combining experimentally measured crystal structures [Fig. 1(a)] with this interpretable probabilistic framework [Fig. 1(c)] enables both accurate prediction and systematic identification of the minimal feature set governing superconductivity. The resulting model, GP- $T_c$ , is made accessible through a web interface [Fig. 1(d)] to enable community-wide materials screening and experimental validation.

The predictive utility of graphlet histograms is illustrated by interatomic-distance distributions across cuprate families [Fig. 2(b)]. Decades of cuprate research established that specific structural parameters—such as the apical Cu–O distance—correlate with  $T_c$  [17–19], but such family-specific descriptors lack generalizability. Our histogram features systematically capture these trends without prior knowledge while remaining applicable across all material classes, demonstrating how structure-aware featurization can unify family-specific empirical observations within a broadly transferable framework.

We curated a featurized database from 3DSC [20], which provides experimentally measured crystal structures and  $T_c$  values. When multiple structures exist for the same composition, we used the Earth Mover’s Distance [15, 16]—a metric quantifying distributional dissimilarity—to retain only materials with consistent representations (normalized EMD < 0.2), yielding 4,325 materials for training both  $T_c$  prediction and superconductivity classification (SM Sec. II.A).

To extract interpretable structure–property relationships from graphlet histograms, we employ Gaussian processes (GPs)—a class of probabilistic machine-learning models that provide not only predictions but also quantified uncertainties and direct measures of feature importance [21–23]. Unlike neural networks that return only point estimates, GPs learn a distribution over functions consistent with the training data, naturally encoding prediction confidence and enabling systematic identification of which features drive model behavior through learned length scales  $\ell_n$  (shorter length scales indicate greater predictive power). This interpretability is essential for our framework: it allows identification of the minimal set of physical descriptors governing superconductivity and quantification of prediction reliability when screening untested materials — capabilities that proved critical for guiding the experimental synthesis pathway for GP- $T_c$  predictions.

The central technical challenge in constructing GP- $T_c$  lies in developing a valid GP kernel for histogram features. Standard kernels assume Euclidean feature vectors, but histograms require distance metrics that respect distributional structure. We employ the Earth Mover’s Distance (EMD) [16], which quantifies the minimum cost of transforming one distribution into another. However, EMD does not directly yield a valid Mercer

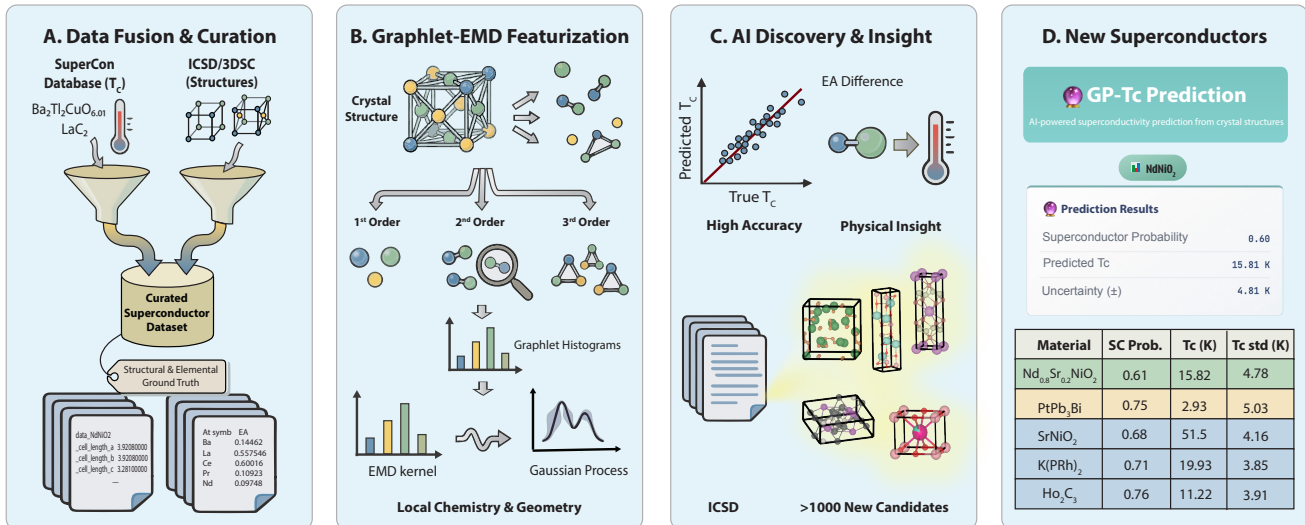


FIG. 1. **Structure-aware machine learning discovers superconductors and reveals organizing principles.** (a) Data from known superconductors and tested non-superconductors are curated from the 3DSC database, incorporating crystal structures (from ICSD), measured transition temperatures ( $T_c$ ), and elemental properties. (b) Materials are encoded as graphlet histograms capturing local bonding environments at multiple scales (1st order: individual atoms; 2nd order: atom pairs; 3rd order: triplets). Histograms are compared using the Earth Mover’s Distance (EMD) to construct a valid probabilistic kernel. (c) The Gaussian process model (GP- $T_c$ ) achieves  $R^2 = 0.93$  while revealing that electron-affinity difference distributions between neighboring atoms dominate prediction. Feature compression from 67 to 4 descriptors exposes compact organizing principles. The framework screens the Inorganic Crystal Structure Database, predicting over 1,000 new candidates. (d) GP- $T_c$  web interface [13] (top) enables community-wide screening. Experimental validation:  $Nd_{0.8}Sr_{0.2}NiO_2$   $T_c$  reproduced (not in training data);  $PtPb_3Bi$  discovered ( $T_c = 2.98$  K vs. predicted 2.93 K). High-priority candidates (table) include  $SrNiO_2$  ( $T_c = 51.5$  K).

kernel because its Gram matrix is not conditionally negative definite, precluding standard transformations like  $\exp(-EMD^2)$ . We prove (SM Sec. II.B) that for one-dimensional histograms, the function

$$K_{EMD}(x_i, x_j) = \sum_n w_n \exp\left(-\frac{EMD(h_{i,n}, h_{j,n})}{\ell_n}\right), \quad (1)$$

constitutes a valid kernel, where  $x_i = \{h_{i,n}\}$  denotes histogram features for material  $i$ , and  $w_n, \ell_n$  are trainable weights and length scales. This result exploits the equivalence between one-dimensional EMD and L1 distance over cumulative distributions. Combining Eq. (1) with a radial-basis-function kernel for symmetry features yields the complete GP- $T_c$  model, whose trained length scales  $\ell_n$  directly reveal feature importance (see SM Sec. II for more details).

GP- $T_c$  achieves state-of-the-art predictive accuracy while offering capabilities unavailable in prior approaches. Fig. 2(c) shows predicted versus experimental  $T_c$  for the held-out test set, yielding  $R^2 = 0.93$ —performance comparable to a neural network trained on the same features (SM Sec. IV) and exceeding prior composition-based models [6, 9]. This robust performance despite using relatively simple machine-learning architectures validates the efficacy of graphlet histogram

features: systematic encoding of local bonding environments provides a natural representation that captures the essential chemistry and geometry governing superconductivity across diverse material families. The test materials span cuprates, iron-based superconductors, heavy fermions, Chevrel phases, and other families, demonstrating broad applicability.

Beyond predictive accuracy, GP- $T_c$  provides two critical advantages for experimental discovery: quantified uncertainty and interpretable feature importance. As a probabilistic model, GP- $T_c$  inherently estimates prediction confidence—larger uncertainties generally accompany larger errors [Fig. 2(c)]. Hence, the uncertainties can guide the experimentalists to prioritize synthesis efforts toward high-confidence predictions. Moreover, because the measured  $T_c$  is sensitive to sample quality, these uncertainties also guide iterative refinement strategies. This probabilistic framework inherently quantifies prediction reliability, a critical capability for guiding costly materials discovery efforts. Feature interpretability emerges through learned length scales: shorter length scales indicate greater predictive influence. Systematic analysis reveals that second-order graphlet features (encoding neighboring atom pairs) provide most of the predictive power [Fig. 2(d)], with first- and third-order features contributing marginally. This hierarchy highlights

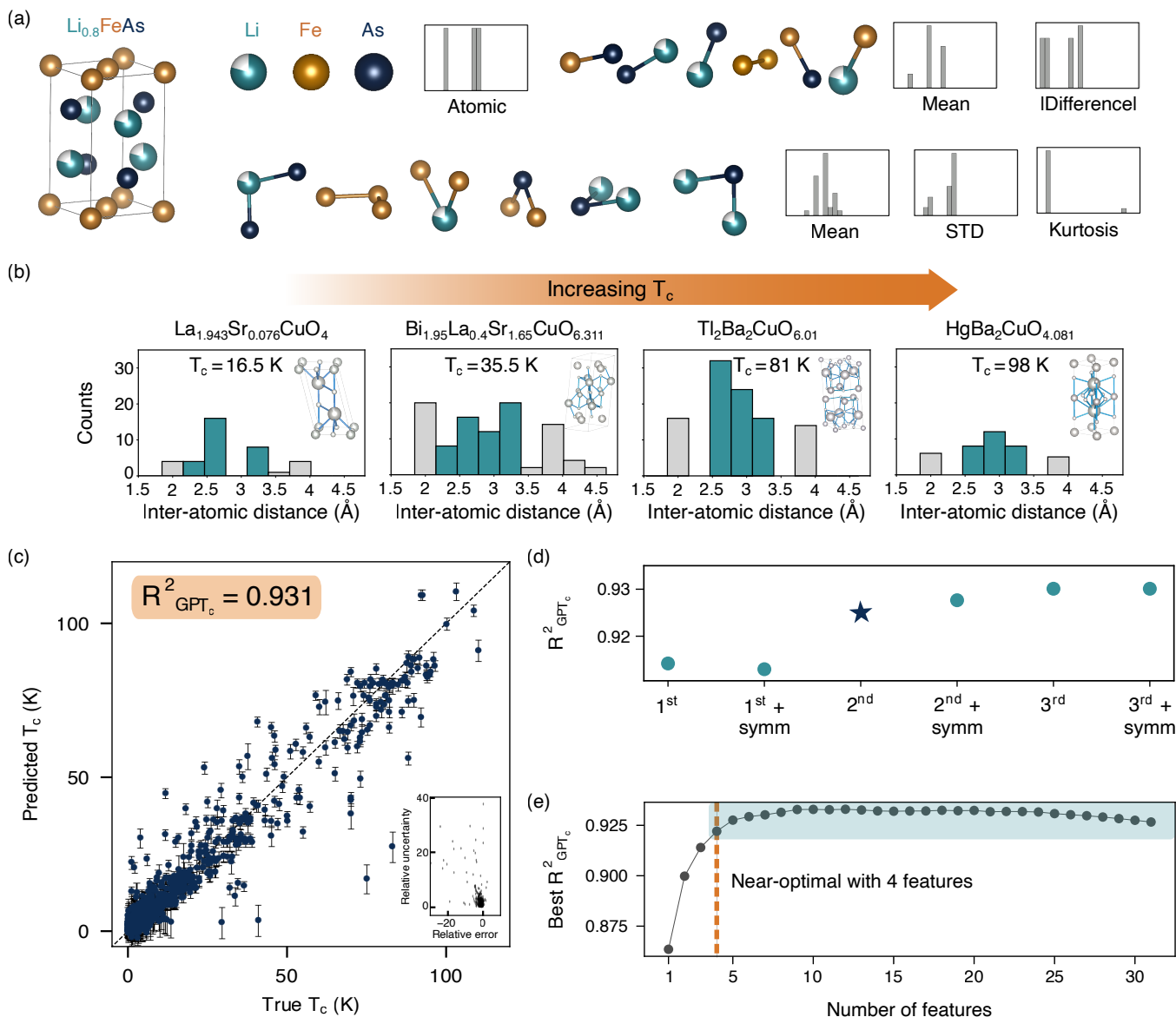


**FIG. 2. Graphlet histograms enable interpretable prediction and reveal dramatic feature compression.** (a) Hierarchical graphlet featurization illustrated with  $\text{Li}_{0.8}\text{FeAs}$ : 1st-order graphlets encode individual atoms (elemental properties), 2nd order encode atom pairs (interatomic distances, elemental means/differences), 3rd-order encode triplets (bond angles, higher-order statistics), generating 67 histogram descriptors per material. (b) Interatomic distance histograms for four cuprate superconductors. Blue bars show interlayer distances varying systematically with  $T_c$ , recovering established correlation between  $T_c$  and apical oxygen distances, but within a universally applicable framework that requires no family-specific parameterization. (c) Predicted versus experimental  $T_c$  for 865 held-out test materials ( $R^2 = 0.931$ ). Error bars show prediction uncertainties. The inset shows that the uncertainties generally correlate with prediction errors. (d) Feature hierarchy: second-order graphlets significantly improve the performance, while symmetry features provide modest improvement. (e) Feature compression: four features achieve near-optimal performance ( $R^2 = 0.922$ ), revealing compact organizing principles.

the importance of pairwise bonding between neighboring sites, validating our chemistry-informed feature design.

The interpretability of  $\text{GP-}T_c$  enables aggressive feature compression. Through iterative pruning—sequentially removing the least informative feature and retraining—we identify that just four features achieve near-optimal performance ( $R^2 = 0.922$ ) [Fig. 2(e)]. To confirm this minimal set, we exhaustively trained  $\text{GP-}T_c$

on all  $\binom{32}{4} = 35,960$  possible four-feature combinations from the 32 second-order and symmetry descriptors (SM Sec. V.A). This dramatic compression from 67 to 4 features suggests that superconductivity, despite its complexity, is governed by surprisingly compact organizing principles—an insight accessible only through the interpretability of the Gaussian process framework, which enables systematic identification of the minimal predic-

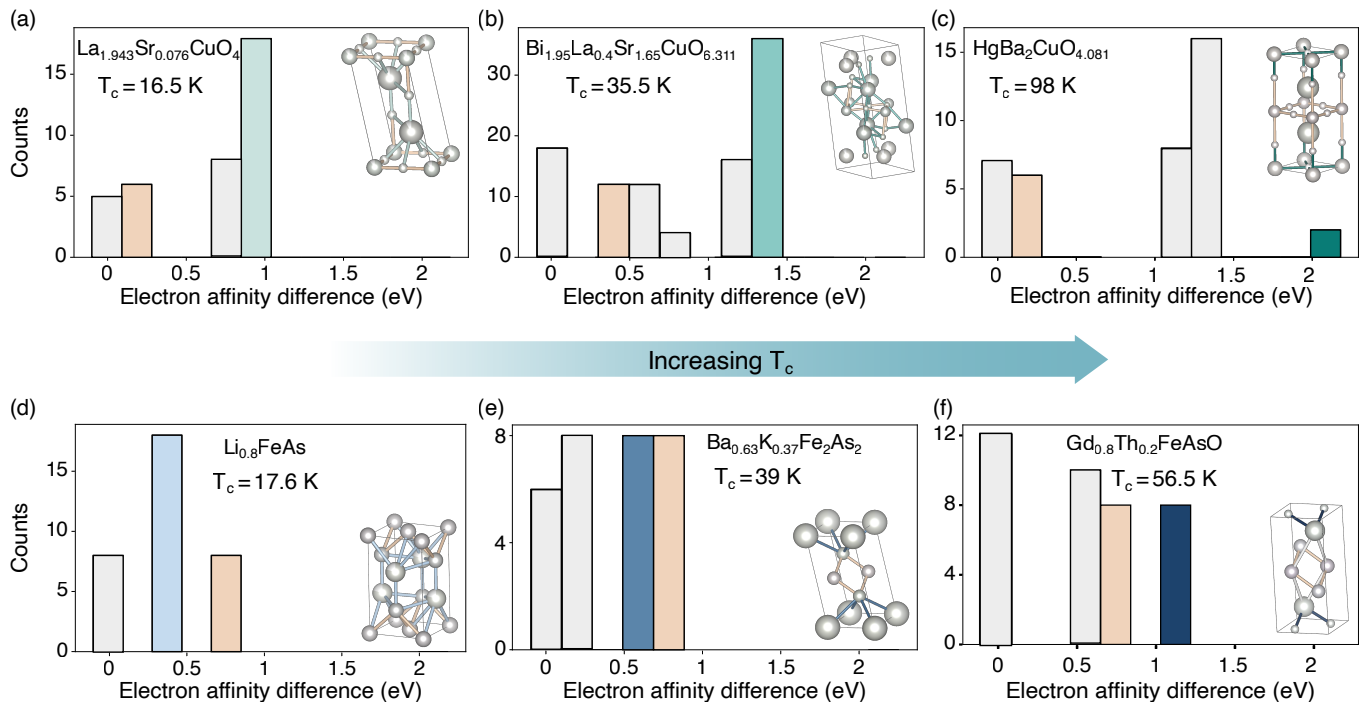


FIG. 3. **Electron affinity difference distributions reveal an organizing principle for superconductivity.** (a–c) Electron affinity (EA) difference histograms for single-layer cuprate superconductors from three families demonstrate systematic trends with  $T_c$ . (a) EA difference histogram for  $\text{La}_{1.943}\text{Sr}_{0.076}\text{CuO}_4$  ( $T_c = 16.5$  K). (b) EA difference histogram for  $\text{Bi}_{1.95}\text{La}_{0.4}\text{Sr}_{1.65}\text{CuO}_{6.311}$  ( $T_c = 35.5$  K). (c) EA difference histogram for  $\text{HgBa}_2\text{CuO}_{4.081}$  ( $T_c = 98$  K). (d–f) Iron-based superconductors exhibit the same trend: broader distributions extending to larger EA differences correlate with higher  $T_c$ . (d) EA difference histogram for  $\text{Li}_{0.8}\text{FeAs}$  ( $T_c = 17.6$  K). (e) EA difference histogram for  $\text{Ba}_{0.63}\text{K}_{0.37}\text{Fe}_2\text{As}_2$  ( $T_c = 39$  K). (f) EA difference histogram for  $\text{Gd}_{0.8}\text{Th}_{0.2}\text{FeAsO}$  ( $T_c = 56.5$  K).

tive feature set and opens pathways to physical understanding.

The exhaustive search over four-feature combinations reveals a consistent pattern. Three sets achieve near-optimal performance ( $R^2 \approx 0.92$ ), all sharing two common descriptors: electron affinity (EA) difference between neighboring atoms and interatomic distance. The third and fourth features vary—periodic table column, valence electron count (total or d-orbital), or atomic weight—but contribute less individually, with notable redundancy among elemental properties (e.g., valence count correlates with periodic table position, as Matthias noted decades ago [2]). Critically, all optimal sets employ exclusively second-order graphlet features, confirming that the pairwise bonding character governs  $T_c$  prediction. Symmetry features, though important for classifying whether materials superconduct, prove insignificant for predicting  $T_c$  itself (SM Sec. IV) [24]. This compressed feature space—where EA difference and interatomic distance provide the core predictive power—enables direct physical interpretation. As noted in Fig. 2(b), interatomic distance histograms systematically encode family-specific structural trends (such as apical oxygen distances in cuprates) within a universally applicable framework.

The emergence of EA difference as the single most in-

formative feature warrants careful consideration. Electron affinity quantifies the energy released when a gas-phase atom gains an electron, a directly measurable atomic property. EA difference histograms between neighboring atoms capture the degree of charge-transfer character in bonding: larger differences indicate more ionic bonds, while smaller differences suggest covalent or metallic character. Historically, superconductivity research focused on Pauling electronegativity (EN)—a theoretical, dimensionless scale combining multiple atomic properties [25–27]—as a proxy for bonding character. Our analysis reveals that EA difference, despite being overlooked in favor of EN, provides superior predictive power. This finding is particularly striking because EA is experimentally accessible, whereas EN is derived.

Examining EA difference distributions across material families [Fig. 3(a–f)] reveals a clear pattern: within cuprates [panels (a–c)] and iron-based superconductors [panels (d–f)], histogram peaks shift toward larger EA differences as  $T_c$  increases across different structural families. The significance of EA difference distribution suggests that bonding heterogeneity—spatial variations in charge-transfer character between different atom pairs—plays a central role in determining superconducting properties, beyond what average or extremal elemental properties capture. The distributional nature of this descrip-

tor, which requires histogram representations rather than scalar summaries, underscores why structure-aware featurization is essential for uncovering this organizing principle.

We now turn to the classification task of distinguishing superconductors from non-superconductors, which plays a central role in prioritizing experimentally actionable candidates. Rather than treating classification as a standalone benchmark problem, we use it as a reliability filter that complements  $GPT_c$  regression. The classifier assigns each material a superconductivity likelihood based on the same structure-aware representation. A balanced dataset labeled with ground-truth labels is ideal for training an accurate classifier. However, the labeled data in 3DSC are imbalanced, with a roughly 2.76:1 ratio of superconductors to tested non-superconductors. Despite this imbalance, predictions correlate strongly with the ground truth [Fig. 4(a)], achieving 82% accuracy for identifying superconductors and 77% for non-superconductors, with the asymmetry reflecting the training data composition (SM Sec. V). These confidence scores, combined with GP- $T_c$  predictions, enable systematic prioritization of synthesis targets.

We now employ the classifier and  $GPT_c$  on all known inorganic crystals in the ICSD outside of 3DSC using four second-order graphlet features [see Fig. 1(d)] to screen their potential for superconductivity, as most materials have not been tested for superconductivity.  $GPT_c$  predicts that over 1,202 crystalline materials exhibit  $T_c > 10$  K outside of 3DSC. Through an exhaustive, AI-based literature search and verification, we confirm that 1,032 materials would be new superconductors if experimentally verified and provide what is known about those materials (see SM Sec. VI and the associated database). Two experimental verifications of the predictions bolster our confidence: the reproduction of  $T_c$  for  $\text{Nd}_{0.8}\text{Sr}_{0.2}\text{NiO}_2$  in the 9–15 K range and our own synthesis and verification of  $\text{PtPb}_3\text{Bi}$ .

The SuperCon database largely preceded the 2018 discovery of superconductivity in the infinite-layer nickelates, and consequently, 3DSC contains no nickelate superconductors, including  $\text{Nd}_{0.8}\text{Sr}_{0.2}\text{NiO}_2$  [28]. In this sense,  $\text{Nd}_{0.8}\text{Sr}_{0.2}\text{NiO}_2$  provides a stringent family-level test for our structure-aware framework:  $GPT_c$  predicts  $T_c$  in the experimentally reported 9–15 K range, and its uncertainty naturally accommodates sample-to-sample variability. Note the prediction assumes homogeneous Sr doping and uniform, single-phase infinite-layer structure, as Ref. [28] found necessary in the reported thin-film superconductivity. The classification confidence is 0.606, reflecting the out-of-distribution nature of the material.

To demonstrate prospective experimental discovery—rather than reproduction of known results—we selected a candidate that was (i) assigned a high superconductivity classification confidence and (ii) experimentally accessible as a stoichiometric ternary compound with readily available elements (SM Sec. VI).  $\text{PtPb}_3\text{Bi}$  [see Fig 4(b)] emerged as such a high-confidence target with classifica-

tion confidence 0.756, with  $GPT_c$  predicting  $T_c \approx 2.93$  K. We synthesized  $\text{PtPb}_3\text{Bi}$  in its pure phase (SM Sec. VI.D) and performed bulk magnetic susceptibility [Fig. 4(c)] and electronic transport [Fig. 4(d)] measurements, which reveal a superconducting transition at  $T_c = 2.98$  K—in excellent agreement with the GP- $T_c$  prediction. The field-cooled susceptibility reaches  $-1.06$  at 1.8 K, confirming a complete superconducting volume fraction. A simplified Werthamer-Helfand-Hohenberg (WHH) fit,  $\mu_0 H_{c2}(0) = -0.693 * T_c * \left. \frac{d\mu_0 H_{c2}}{dT} \right|_{T=T_c}$ , suggests an upper critical field limit of 0.667 T, far below the Pauli limit,  $H_P \approx 1.86 \times 3.0 \approx 5.6$  T, consistent with an orbital-pair breaking mechanism. Temperature- and frequency-dependent  $I - V$  curves, as well as field-dependent magnetization are all consistent with type-II behavior, characteristic of multi-element intermetallics and indicative of bulk superconductivity (see SM Sec. VI). Interestingly,  $\text{PtPb}_3\text{Bi}$  forms a unique structure type, hosting face-sharing dimerized  $[\text{Pt}_2\text{Pb}_8\text{Bi}_4]$  bicapped trigonal prismatic units, stacked along the c-axis forming a quasi-one-dimensional structure type (see SM Sec. VI). To the best of our knowledge, no other variants have been reported among superconductors; this unique structure type would have been overlooked by structure-motif-based or symmetry-constrained search strategies, demonstrating GP- $T_c$ 's ability to discover materials beyond theoretical bias.

Beyond the experimental validation of  $\text{PtPb}_3\text{Bi}$ , our screening of the Inorganic Crystal Structure Database (ICSD) identifies numerous high-priority candidates for experimental investigation. To facilitate community access, we deployed GP- $T_c$  through an interactive web interface. Figure 4(e) displays the screening landscape, with each point representing a predicted material, positioned by its predicted  $T_c$  ( $x$ -axis) and classification confidence ( $y$ -axis). It reveals that the high- $T_c$ , high-confidence upper-right quadrant contains the most compelling experimental targets. Among the 1,032 predicted new superconductors with  $T_c > 10$  K (see SM Sec. VI and associated database), several particularly intriguing examples emerge. Most notably,  $\text{SrNiO}_2$  receives a predicted  $T_c = 51.5$  K (uncertainty  $\pm 4.16$  K, classification confidence 0.67)—substantially higher than any known nickelate superconductor. This prediction is especially tantalizing given that Sr doping enables superconductivity in  $\text{Nd}_{0.8}\text{Sr}_{0.2}\text{NiO}_2$  by introducing holes into the insulating parent  $\text{NdNiO}_2$ . Little is known about  $\text{SrNiO}_2$ , with only one paper reporting the preparation of single crystals of  $\text{SrNiO}_2$  [29]; we used the reported tetragonal CmCm structure in our prediction. [30] The high predicted  $T_c$  suggests that the stoichiometric compound and its electron-doped variants warrant systematic investigation. Other high-confidence predictions include  $\text{K}(\text{PRh})_2$  and  $\text{Ho}_2\text{C}_3$  [highlighted in Fig. 1(d)], providing concrete experimental targets across diverse chemical families.

To summarize, we introduced a structure-aware and interpretable framework for superconductivity prediction that explicitly integrates elemental chemistry with local

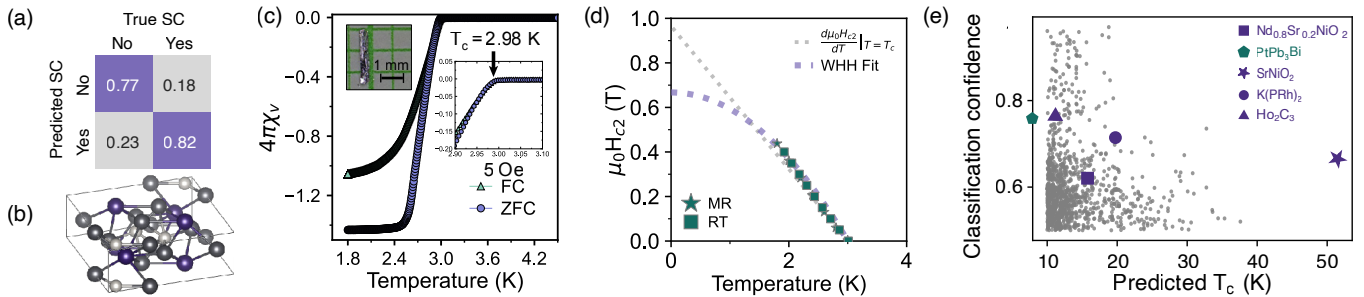


FIG. 4. **Experimental validation confirms GP- $T_c$  predictions and identifies high-priority candidates.** Classification confidence, combined with the predicted  $T_c$ , guides experimental discovery. (a) Confusion matrix for GP-based superconductivity classifier on held-out test data, achieving 82% accuracy for superconductors and 77% for non-superconductors. (b) Crystal structure of PtPb<sub>3</sub>Bi (space group P4<sub>2</sub>/mnm). (c) Magnetic susceptibility versus temperature for PtPb<sub>3</sub>Bi showing superconducting transition at  $T_c = 2.98$  K, matching predicted 2.93 K. The field-cooled curve reaches  $-1.06$  at 1.8 K, indicating a complete volume fraction. The inset shows the synthesized sample. (d) Electronic transport confirms a bulk superconducting transition. A simplified Werthamer-Helfand-Hohenberg (WHH) fit suggests an upper critical field  $\mu_0 H_{c2}(0) \approx 0.667$  T. (e) Predicted new superconductors with  $T_c > 10$  K. Highlighted materials include validated Nd<sub>0.8</sub>Sr<sub>0.2</sub>NiO<sub>2</sub> (square, outside training data), high-priority targets SrNiO<sub>2</sub> (star,  $T_c = 51.5$  K), K(PRh)<sub>2</sub> (circle), and Ho<sub>2</sub>C<sub>3</sub> (triangle). PtPb<sub>3</sub>Bi’s position (marked in teal on the y-axis) demonstrates that materials with moderate confidence can yield validated discoveries.

bonding geometry derived from experimentally measured crystal structures. By encoding materials using graphlet histograms and learning within a Gaussian process model (GP- $T_c$ ), we achieve accurate, uncertainty-quantified predictions of both superconductivity and  $T_c$  while retaining direct access to the physical features that govern model behavior. This design choice enables not only predictive performance but also the extraction of compact, chemically meaningful organizing principles.

A central outcome of this approach is the dramatic compression of the predictive feature space. We find that the distribution of electron-affinity differences between neighboring atoms, together with a small number of elemental and structural descriptors, suffices to achieve near-optimal performance in  $T_c$  prediction. That such a readily available and directly measurable quantity emerges as the most informative feature highlights the central role of local bonding character in superconductivity. This result shifts attention away from opaque high-dimensional descriptors toward chemically interpretable variables that can be directly connected to bonding physics and materials design.

Beyond insight, GP- $T_c$  demonstrates reliable experimental actionability. We reproduce the superconducting behavior of the recently established infinite-layer nickelate family and predict and experimentally confirm superconductivity in stoichiometric PtPb<sub>3</sub>Bi, establishing a new superconductor. At the same time, the framework identifies multiple additional high-priority candidates, including SrNiO<sub>2</sub> with a predicted  $T_c$  of 51.5 K, providing concrete targets for experimental exploration. By making GP- $T_c$  accessible through a web interface [13] that enables structure-based prediction from standard CIF files, we aim to lower the barrier to community-wide exploration. More broadly, because the featurization relies only on fundamental elemental and structural informa-

tion, the strategy developed here is readily extensible to other material properties, opening a path toward interpretable, data-driven discovery across quantum materials.

**Author Contributions:** E.-A.K. and J.G. planned the machine learning strategy and guided the research activities. K.M. devised the graphlet expansion and the EMD metric. N.M. built the EMD kernel and trained the GP models. O.L. carried out NN-based studies and led the interpretation efforts. Y.L. designed the symmetry features and analyzed ML results. Y.L. and A.P. wrote the code for graphlet and symmetry feature generation and curated the database. A.P. implemented the prediction pipeline for the ICSD screening. A.P. and O.L. compiled the predicted superconducting candidates. A.P. implemented the GP- $T_c$  prediction web interface. A.G. and A.K. developed the literature-search tools used to analyze the predicted superconducting materials. K.W. advised an LLM-based comprehensive literature search to identify precedents for GP- $T_c$  predictions. A.G. and A.K. designed and carried out the LLM-based comprehensive literature search to identify precedents for GP- $T_c$  predictions. L.S. advised the choice of atomistic features, the classification experiments, the choice of PtPb<sub>3</sub>Bi as the first test case material, its synthesis, its characterization, and its measurements. S.L., S.C., and A.M. synthesized, characterized, and measured PtPb<sub>3</sub>Bi.

**Acknowledgements:** We are grateful to Andrei Bernevig, Timo Sommer, Pascal Friederich, Jörg Schmalian, Ichiro Takeuchi, and Steve Kivelson for helpful discussions. E.-A.K., K.W., and L.S. are supported by the NSF through the AI Research Institutes program Award No. DMR-2433348 and by the grant OAC-2118310. Y.L. and E.-A.K. were supported in part by the MURI grant FA9550-21-1-0429. K.M. was supported by Eric and Wendy Schmidt AI in Science Postdoctoral Fel-

lowship: a Schmidt Futures program. The computation was performed on a high-performance computing cluster supported by the Gordon and Betty Moore Foundation's EPiQS Initiative, Grant GBMF10436 to E.-A.K., and by the MURI grant FA9550-21-1-0429. K.M., Y.L., and E.-A.K. are supported by the U.S. Department of Energy, Office of Science, Basic Energy Sciences, Materials Sciences and Engineering Division. O.L. and E.-A.K. are supported by the U.S. Department of Energy through Award Number DE-SC0023905. O.L. is also supported by a Bethe-KIC postdoctoral fellowship at Cornell University. J.G. was supported by NSF grants DBI-2400135 and IIS-2145644. N.M. was supported by an NSF Gradu-

ate Research Fellowship. S.L. and S.C. are supported by the Air Force Office of Scientific Research under award number FA9550-25-1-0177. A.M. was supported by an NSF CAREER grant (DMR-2144295) to L.S.

**Data and code availability:** Featurized training data supporting the findings of this study, provided as graphlet histograms, together with code implementing the full data pipeline, including crystal structure graphlet featurization, Gaussian process model training, and prediction, are available at upon request from the authors. Raw crystal structure inputs are subject to licensing restrictions from the Inorganic Crystal Structure Database (ICSD) and cannot be redistributed.

- 
- [1] G. M. Eliashberg, Interactions between electrons and lattice vibrations in a superconductor, *Sov. Phys. - JETP (Engl. Transl.)*; (United States) **11:3** (1960).
- [2] B. T. Matthias, Chapter V: Superconductivity in the Periodic System, in *Progress in Low Temperature Physics*, Vol. 2, edited by C. J. Gorter (Elsevier, 1957) pp. 138–150.
- [3] *SuperCon*, <https://doi.org/10.48505/nims.3837> (2022).
- [4] V. Stanev, C. Oses, A. G. Kusne, E. Rodriguez, J. Paglione, S. Curtarolo, and I. Takeuchi, Machine learning modeling of superconducting critical temperature, *npj Computational Materials* **4**, 29 (2018).
- [5] S. Li, Y. Dan, X. Li, T. Hu, R. Dong, Z. Cao, and J. Hu, Critical Temperature Prediction of Superconductors Based on Atomic Vectors and Deep Learning, *Symmetry* **12**, 262 (2020).
- [6] T. Konno, H. Kurokawa, F. Nabeshima, Y. Sakishita, R. Ogawa, I. Hosako, and A. Maeda, Deep learning model for finding new superconductors, *Physical Review B* **103**, 014509 (2021).
- [7] K. Hamidieh, A data-driven statistical model for predicting the critical temperature of a superconductor, *Computational Materials Science* **154**, 346 (2018).
- [8] K. Matsumoto and T. Horide, An acceleration search method of higher  $T_c$  superconductors by a machine learning algorithm, *Applied Physics Express* **12**, 073003 (2019).
- [9] C. Pereti, K. Bernot, T. Guizouarn, F. Laufek, A. Vymazalová, L. Bindi, R. Sessoli, and D. Fanelli, From individual elements to macroscopic materials: In search of new superconductors via machine learning, *npj Computational Materials* **9**, 71 (2023).
- [10] K. Choudhary and B. DeCost, Atomistic Line Graph Neural Network for improved materials property predictions, *npj Computational Materials* **7**, 185 (2021).
- [11] J. B. Gibson, A. C. Hire, P. M. Dee, B. Geisler, J. S. Kim, Z. Li, J. J. Hamlin, G. R. Stewart, P. J. Hirschfeld, and R. G. Hennig, *Developing a Complete AI-Accelerated Workflow for Superconductor Discovery* (2025), [arXiv:2503.20005 \[cond-mat\]](https://arxiv.org/abs/2503.20005).
- [12] K. Choudhary and K. Garrity, Designing high-TC superconductors with BCS-inspired screening, density functional theory, and deep-learning, *npj Computational Materials* **8**, 244 (2022).
- [13] Web-based interface access is available upon request from the authors.
- [14] T. F. T. Cerqueira, A. Sanna, and M. A. L. Marques, Sampling the Materials Space for Conventional Superconducting Compounds, *Advanced Materials* **36**, 2307085 (2024).
- [15] Y. Rubner, C. Tomasi, and L. J. Guibas, The Earth Mover's Distance as a Metric for Image Retrieval, *International Journal of Computer Vision* **40**, 99 (2000).
- [16] P. T. Komiske, E. M. Metodiev, and J. Thaler, Metric Space of Collider Events, *Physical Review Letters* **123**, 041801 (2019).
- [17] C. Rao and A. Ganguli, Relation between superconducting properties and structural features of cuprate superconductors, *Physica C: Superconductivity* **235–240**, 9 (1994).
- [18] E. Pavarini, I. Dasgupta, T. Saha-Dasgupta, O. Jepsen, and O. K. Andersen, Band-Structure Trend in Hole-Doped Cuprates and Correlation with  $T_{c\max}$ , *Physical Review Letters* **87**, 047003 (2001).
- [19] E.-M. Choi, A. Di Bernardo, B. Zhu, P. Lu, H. Alpern, K. H. L. Zhang, T. Shapira, J. Feighan, X. Sun, J. Robinson, Y. Paltiel, O. Millo, H. Wang, Q. Jia, and J. L. MacManus-Driscoll, 3D strain-induced superconductivity in  $\text{La}_2\text{CuO}_{4+\delta}$  using a simple vertically aligned nanocomposite approach, *Science Advances* **5**, eaav5532 (2019).
- [20] T. Sommer, R. Willa, J. Schmalian, and P. Friederich, 3DSC - a dataset of superconductors including crystal structures, *Scientific Data* **10**, 816 (2023).
- [21] F. Vivarelli and C. Williams, Discovering hidden features with gaussian processes regression, in *Advances in Neural Information Processing Systems*, Vol. 11, edited by M. Kearns, S.olla, and D. Cohn (MIT Press, 1998).
- [22] C. E. Rasmussen and C. K. I. Williams, *Gaussian Processes for Machine Learning*, Adaptive Computation and Machine Learning (MIT Press, Cambridge, Mass, 2006).
- [23] J. Hensman, N. Fusi, and N. D. Lawrence, Gaussian processes for big data, *Uncertainty in Artificial Intelligence* (2013).
- [24] The symmetry features play a more prominent role in predicting whether a material will superconduct (see SM Sec. IV).
- [25] Q.-G. Luo and R.-Y. Wang, Electronegativity and superconductivity, *Journal of Physics and Chemistry of Solids*

- 48, 425 (1987).
- [26] R. Jayaprakash and J. Shanker, Correlation between electronegativity and high temperature superconductivity, *Journal of Physics and Chemistry of Solids* **54**, 365 (1993).
- [27] K. M. Rabe, J. C. Phillips, P. Villars, and I. D. Brown, Global multinary structural chemistry of stable quasicrystals, high- $T_C$  ferroelectrics, and high- $T_c$  superconductors, *Physical Review B* **45**, 7650 (1992).
- [28] D. Li, K. Lee, B. Y. Wang, M. Osada, S. Crossley, H. R. Lee, Y. Cui, Y. Hikita, and H. Y. Hwang, Superconductivity in an infinite-layer nickelate, *Nature* **572**, 624 (2019).
- [29] H. Pausch and H. Mueller-Buschbaum, Preparation of single crystals of SrNiO<sub>2</sub> with coplanar coordinated nickel, *Z. Anorg. Allg. Chem.* **426**, 184–188 (1976).
- [30] Wang et al predicted Hunds metal at 100K for the infinite layer P4/mmm structure. However, (La,Sr)NiO<sub>2</sub> system which was also predicted to be Hunds metal have recently been confirmed to be superconducting at 9K. [31].
- [31] M. Osada, B. Y. Wang, B. H. Goodge, S. P. Harvey, K. Lee, D. Li, L. F. Kourkoutis, and H. Y. Hwang, Nickelate superconductivity without rare-earth magnetism: (la,sr)nio2, *Advanced Materials* **33**, 2104083 (2021).
- [32] S. Zeng, Y. Zhao, G. Li, R. Wang, X. Wang, and J. Ni, Atom table convolutional neural networks for an accurate prediction of compounds properties, *npj Computational Materials* **5**, 84 (2019).
- [33] B. Roter and S. Dordevic, Predicting new superconductors and their critical temperatures using machine learning, *Physica C: Superconductivity and its Applications* **575**, 1353689 (2020).
- [34] T. D. Le, R. Noumeir, H. L. Quach, J. H. Kim, J. H. Kim, and H. M. Kim, Critical Temperature Prediction for a Superconductor: A Variational Bayesian Neural Network Approach, *IEEE Transactions on Applied Superconductivity* **30**, 1 (2020).
- [35] *Inorganic Crystal Structure Database*, <https://icsd.products.fiz-karlsruhe.de/> (1978).
- [36] D. Zagorac, H. Müller, S. Ruehl, J. Zagorac, and S. Rehme, Recent developments in the Inorganic Crystal Structure Database: theoretical crystal structure data and related features, *Journal of Applied Crystallography* **52**, 918 (2019).
- [37] A. Jain, S. P. Ong, G. Hautier, W. Chen, W. D. Richards, S. Dacek, S. Cholia, D. Gunter, D. Skinner, G. Ceder, and K. A. Persson, Commentary: The materials project: A materials genome approach to accelerating materials innovation, *APL Materials* **1**, 011002 (2013), <https://pubs.aip.org/aip/apm/article-pdf/doi/10.1063/1.4812323/13163869/011002.1.online.pdf>.
- [38] S. P. Ong, W. D. Richards, A. Jain, G. Hautier, M. Kocher, S. Cholia, D. Gunter, V. L. Chevrier, K. A. Persson, and G. Ceder, Python Materials Genomics (pymatgen): A robust, open-source python library for materials analysis, *Computational Materials Science* **68**, 314 (2013).
- [39] J. C. Slater, Atomic radii in crystals, *The Journal of Chemical Physics* **41**, 3199 (1964), <https://pubs.aip.org/aip/jcp/article-pdf/41/10/3199/18835412/3199.1.online.pdf>.
- [40] J. R. Rumble, T. J. Bruno, and M. J. Doa, eds., *CRC Handbook of Chemistry and Physics: A Ready-Reference Book of Chemical and Physical Data*, 101st ed. (CRC Press, Taylor & Francis Group, Boca Raton London New York, 2020).
- [41] W. C. Martin, A. Musgrove, S. Kotochigova, and J. E. Sansonetti, *Ground levels and ionization energies for the neutral atoms*, Online; Version 1.3 (2011), accessed 2025-09-28.
- [42] J. Meija, T. B. Coplen, M. Berglund, W. A. Brand, P. D. Bièvre, M. Gröning, N. E. Holden, J. Irrgeher, R. D. Loss, T. Walczyk, and T. Prohaska, Atomic weights of the elements 2013 (iupac technical report), *Pure and Applied Chemistry* **88**, 265 (2016).
- [43] S. Batzner, A. Musaelian, L. Sun, M. Geiger, J. P. Mailoa, M. Kornbluth, N. Molinari, T. E. Smidt, and B. Kozinsky, E(3)-equivariant graph neural networks for data-efficient and accurate interatomic potentials, *Nature communications* **13**, 2453 (2022).
- [44] M. Geiger and T. Smidt, *e3nn: Euclidean neural networks* (2022), [arXiv:2207.09453 \[cs.LG\]](https://arxiv.org/abs/2207.09453).
- [45] M. I. Aroyo, ed., *International Tables for Crystallography, Volume A: Space-Group Symmetry*, 2nd ed. (2016).
- [46] R. Flamary, N. Courty, A. Gramfort, M. Z. Alaya, A. Boisbunon, S. Chambon, L. Chapel, A. Corenflos, K. Fatras, N. Fournier, L. Gautheron, N. T. Gayraud, H. Janati, A. Rakotomamonjy, I. Redko, A. Rolet, A. Schutz, V. Seguy, D. J. Sutherland, R. Tavenard, A. Tong, and T. Vayer, POT: Python optimal transport, *Journal of Machine Learning Research* **22**, 1 (2021).
- [47] M. Martinez, M. Tapaswi, and R. Stiefelhagen, A closed-form gradient for the 1d earth mover’s distance for spectral deep learning on biological data, in *ICML 2016 Workshop on Computational Biology (CompBio@ICML16)* (2016).
- [48] J. E. Hirsch, Correlations between normal-state properties and superconductivity, *Physical Review B* **55**, 9007 (1997).
- [49] A. Jain, S. P. Ong, G. Hautier, W. Chen, W. D. Richards, S. Dacek, S. Cholia, D. Gunter, D. Skinner, G. Ceder, and K. A. Persson, Commentary: The Materials Project: A materials genome approach to accelerating materials innovation, *APL Materials* **1**, 011002 (2013).
- [50] J. M. Munro, K. Latimer, M. K. Horton, S. Dwaraknath, and K. A. Persson, An improved symmetry-based approach to reciprocal space path selection in band structure calculations, *npj Computational Materials* **6**, 112 (2020).
- [51] M. D. Skarlinski, S. Cox, J. M. Laurent, J. D. Braza, M. Hinks, M. J. Hammerling, M. Ponnepati, S. G. Rodrigues, and A. D. White, Language agents achieve superhuman synthesis of scientific knowledge, *arXiv preprint arXiv:2409.13740* (2024).
- [52] C. J. Lygouras, J. Zhang, J. Gautreau, M. Pula, S. Sharma, S. Gao, T. Berry, T. Halloran, P. Orban, G. Grissonnanche, J. R. Chamorro, T. Mikuri, D. K. Bhoi, M. A. Siegler, K. J. Livi, Y. Uwatoko, S. Nakatsuji, B. J. Ramshaw, Y. Li, G. M. Luke, C. L. Broholm, and T. M. McQueen, Type i and type ii superconductivity in a quasi-2d dirac metal, *Mater. Adv.* **6**, 1685 (2025).
- [53] R. Prozorov and V. G. Kogan, Effective demagnetizing factors of diamagnetic samples of various shapes, *Phys. Rev. Appl.* **10**, 014030 (2018).
- [54] C. Q. Xu, B. Li, L. Zhang, J. Pollanen, X. L. Yi, X. Z. Xing, Y. Liu, J. H. Wang, Z. Zhu, Z. X. Shi, X. Xu, and X. Ke, Superconductivity in ptpb<sub>4</sub> with possible nontrivial band topology, *Phys. Rev. B* **104**, 125127 (2021).

- [55] L.-M. Wang, S.-E. Lin, D. Shen, and I.-N. Chen, Normal-state negative longitudinal magnetoresistance and dirac-cone-like dispersion in ptpb4 single crystals: a potential weyl-semimetal superconductor candidate, *New Journal of Physics* **23**, 093030 (2021).
- [56] P. GarcíaTalavera, J. A. Moreno, E. Herrera, A. I. Buzdin, S. L. Bud'ko, P. C. Canfield, I. Guillamón, and H. Suderow, Superconducting density of states of ptpb4, *Journal of Superconductivity and Novel Magnetism* **38**, 158 (2025).

# Supplementary Material for “Electron affinity difference distributions guide the discovery of the superconductor PtPb<sub>3</sub>Bi”

## I. DATA AND FEATURES

In most ML works focusing on superconductivity, the data came from the SuperCon database, which tabulates the experimental measurements of superconductivity for >16000 materials and their references [3, 4, 6–9, 32–34]. For ML studies, the applicable data in SuperCon are only the chemical formula and critical temperatures of the materials. Furthermore, some materials have multiple entries reported by different references with varying reported  $T_c$  values. The lack of structural information restricted previous works to composition-only features, eliminating the possibility for the ML algorithms to uncover structure-related mechanisms of the problem. Here we describe a way to leverage more information about the materials, using an enhanced database that recently became available.

### A. 3DSC down selection

In this work, we collected the chemical formulas and  $T_c$  information of materials from the 3DSC database [20]. We collected Crystallographic Information Files (CIFs) of the materials from the Inorganic Crystal Structure Database (ICSD) [35, 36], with their collection codes provided in 3DSC. The 3DSC database contains the critical temperatures and approximated crystal structures of experimentally measured superconducting and non-superconducting materials. The key idea is to match materials in the SuperCon database with crystal structures from the Materials Project (MP) [37] or the ICSD, with some artificial modifications when necessary. Thus, 3DSC has two datasets, 3DSC<sub>MP</sub> and 3DSC<sub>ICSD</sub>. In this work, we focus on the 3DSC<sub>ICSD</sub> dataset, which relies primarily on experimental data rather than on first-principles calculations. 3DSC<sub>ICSD</sub> includes approximately 57% of the SuperCon entries (9150 materials). However, many of the materials are matched with multiple CIFs, in which the recorded crystal structures are not necessarily identical. Two main reasons cause the variances of recorded crystal structures of a single chemical formula. First, the material may exhibit polymorphism. Second, the exact same material does not exist in the ICSD, and the crystal structures are obtained by doping different parent materials in the ICSD with similar chemical compositions but different structures. Since our material featurization encodes structural information, and there is generally no evidence to favor one structure over another, we develop a quantitative criterion to further filter materials that we can work with from 3DSC<sub>ICSD</sub>.

Our selection criterion is based on graphlet features and Earth Mover’s Distances (EMD), both of which will be detailed in the following sections. After graphlet featurization, we obtained valid histogram features for 76,037 CIFs that come from 8,781 materials. Among them, 57,274 CIFs come from 6,463 superconductors with non-zero  $T_c$ s. For the regression ( $T_c$  prediction) data, we include only superconductors. First, we selected all the 2,033 superconductors with a unique CIF. To enlarge the dataset, we also want to include superconductors that have multiple CIFs associated with each one. There are two primary reasons for this multiplicity: (1) identical crystal structures may be reported by different references, producing multiple but nearly identical CIFs; and (2) the material may exhibit polymorphism or the CIFs are doped from different parent materials through the 3DSC doping algorithm, which will result in actually distinct CIFs. To ensure the quality of our dataset, we only select the superconductors that have multiple but similar CIFs.

We measure whether the set of CIFs for one superconductor is similar by calculating the EMDs between histogram features. After graphlet featurization, each CIF is represented by 10 first-order histogram features and 21 second-order histogram features. We first calculated EMDs for every pair of the 2,033 unique-CIF superconductors, resulting in 2,065,528 EMD samples per feature. For each feature dimension, we sorted the EMD values and defined the 1st percentile as the similarity threshold. Two CIFs are considered similar if their EMDs in all 31 histogram features fall below the respective thresholds.

Using this criterion, we evaluated all pairs of the 2,033 superconductors with unique CIFs. Out of 2,065,528 pairs, 908 were identified as similar—implying that 99.96% of non-similar pairs were correctly classified. We then applied the same criterion to superconductors with multiple CIFs. If all pairwise comparisons among a material’s CIFs satisfied the similarity condition, we retained that material and arbitrarily selected one of its CIFs, as they were deemed sufficiently alike. This process added 2,292 superconductors to the dataset, bringing the total to 4,325 superconductors. For the 2318 non-superconductors with 18763 CIFs, we went through the same process and obtained 1531 non-superconductors for classification.

This curation step ensures that learned trends reflect intrinsic material properties rather than artifacts of structural uncertainty. Equipped with the featurized database and ground truth  $T_c$ , we train ML models for two different

supervised learning tasks:  $T_c$  prediction and superconductivity prediction. The entire dataset is randomly split into 80% training and 20% testing sets. The model parameters are optimized to minimize training error, and performance is assessed on the test set.

### B. Artificial doping procedure used in 3DSC

Most chemical formulas in the SuperCon database are non-stoichiometric and therefore lack exact counterparts in the ICSD database. To increase the number of matched entries, the 3DSC people consider not only exact formula matches but also ICSD entries whose formulas are sufficiently similar to those in SuperCon, as quantified by several stoichiometry-based metrics detailed in their paper [20]. When two formulas are deemed similar but not identical, the authors apply their artificial-doping algorithm to the ICSD CIF to adjust site occupancies and tune the composition. This yields a hypothetical CIF whose composition matches the SuperCon entry exactly, and 3DSC records the hypothetical CIF together with the formula and  $T_c$  from the SuperCon database.

Artificial doping starts from an ICSD crystal structure with a similar chemical formula, which serves as a proxy for the SuperCon entry’s actual structure. The algorithm then partially replaces the atoms at specified crystallographic sites with other elements. It handles statistically occurring vacancies by treating “nothing” as the dopant and reducing the occupancy of the corresponding site. Only site occupancies are modified—atomic coordinates and interatomic distances remain unchanged. The assumption is that the original formulas are sufficiently close, so the real structure in SuperCon is likely to share similar crystallographic parameters.

To perform artificial doping, three additional requirements must be met: (a) Each dopant must map to a unique set of equivalent crystal sites. A “set of equivalent crystal sites” comprises sites sharing the same Wyckoff position. This condition is satisfied in any of the following situations: (i) the host element fully occupies exactly one set of equivalent sites and does not partially occupy any other site set; (ii) the host element partially occupies exactly one set of equivalent sites—it may also fully occupy one or more other site sets, which are ignored; (iii) the host element partially occupies more than one set of equivalent sites, but with identical occupancies—again, any additional fully occupied site sets are ignored. (b) The replacement must not create any site containing more than two elements. (c) Artificial doping must not add or remove crystal sites. With these criteria, artificial doping can be applied to complex compounds, including a large number of cuprates. The detailed code is available at: <https://github.com/aimat-lab/3DSC>.

### C. Graphlet feature generation from atomic properties

In this work, we introduce a hierarchical graphlet expansion for material featurization (see Github for details). This framework begins with the CIFs of materials and selected elemental properties and encodes both chemical and structural information in a systematic and holistic manner.

The concept of graphlet expansion originated in biological network analysis, where biological entities such as proteins or genes are represented as identical nodes, and graphlets are defined as small connected subgraphs. The frequency of these subgraphs serves as a key descriptor for characterizing complex biological networks. In those applications, only the topology of the graphlets is typically considered, while the specific properties of the actual entities represented by the nodes are often discarded. However, in material featurization, we are interested in not only the local connectivities between different atoms, but also the chemical properties and geometry. To adopt graphlets to our context, we make two main enhancements. First, we retain the identities of different atoms when constructing the graphlets. Second, we use graphlets as the basis for encoding local chemical and structural properties, instead of simply recording the frequencies of different graphlets as the feature. In the following, we describe the details in steps (see Github for details).

Structural representations of non-stoichiometric materials are necessarily approximate. Nevertheless, a significant fraction (65%) of superconducting materials are doped materials in which carriers are introduced to achieve an average density. When an element substitutes another element at a fractional rate, we treat the site in question as occupied by an “average” atom whose elemental properties are weighted averages. This approach leaves out changes in inter-site distances upon doping. Furthermore, uncertainties on the exact location of dopants are handled only on average. Surprisingly, such baseline features turn out to be sufficient for our trained models to reach a high accuracy of  $R_{\text{opt}}^2 > 0.93$ , as we show later.

*Step 1:* We begin by reading the CIF of a material and identifying its primitive unit cell [38]. We then examine all atomic sites within the cell. For each site, we record the chemical elements and occupancy information (in cases involving doping or vacancies) and search for its nearest neighbors using the VoronoiNN algorithm. The nearest neighbors involve those from neighboring primitive cells. We collect the list of all valid nearest neighbors and their composition information. A nearest-neighbor site is considered valid if it lies within a cutoff distance to the center

site, defined as 1.5 times the sum of the atomic radii of the two sites. We used the empirical atomic radii published by Slater [39]. If a site is partially occupied – either due to doping or the presence of vacancies – then its effective atomic radius is calculated as the weighted average of the atomic radii of all constituent species, with each atomic radius weighted by its site occupancy. For example, in the doped material  $\text{Mg}_{0.95}\text{Al}_{0.05}\text{B}_2$ , the B atoms occupy the 2d sites with an effective atomic radius of 85 pm. The 1a site, occupied by Mg and Al, has a weighted average effective radius calculated as  $(0.95 \times 150 \text{ pm}) + (0.05 \times 125 \text{ pm}) = 148.75 \text{ pm}$ .

*Step 2:* We iteratively examine all atomic sites and their valid neighbors, and construct the complete sets of the first-order graphlets, the second-order graphlets, and the third-order graphlets. We define a first-order graphlet as a single crystal site. Accordingly, the complete set of first-order graphlets comprises all inequivalent sites in the primitive cell. A second-order graphlet is defined as a valid pair of neighboring sites, and the complete set of second-order graphlets includes all inequivalent such pairs. Finally, a third-order graphlet is defined as a center site and two of its valid neighbors. The two neighbors are not necessarily valid neighbors to each other. The complete set of third-order graphlets collects all inequivalent such triangles. A graphical illustration of the first-order, second-order, and third-order graphlets is shown in Fig. S1.

TABLE S1. List of elemental properties used for constructing chemical features.

Property	Description	Source	Method
EN	Pauling electronegativity	CRC Handbook of Chemistry and Physics [40]	Based on measurement (semi-empirical)
EA	Electron affinity (eV)	CRC Handbook of Chemistry and Physics	Measured; few elements are calculated
IP	Ionization potential (eV)	NIST Atomic Spectra Database Ionization Energies Form [41]	Measured; few elements are calculated
$R_{\text{cov}}$	Covalent radius (pm)	CRC Handbook of Chemistry and Physics	Based on measurement; few elements are calculated
AW	Atomic weight	Atomic weights of the elements 2013 [42]	Based on measurement
$N_s$	Valence electrons in <i>s</i>	Periodic Table	Determined from the periodic table
$N_p$	Valence electrons in <i>p</i>	Periodic Table	Determined from the periodic table
$N_d$	Valence electrons in <i>d</i>	Periodic Table	Determined from the periodic table
$N_{\text{tot}}$	Total valence electrons	Periodic Table	Determined from the periodic table
Col	Column number in periodic table	Periodic Table	Determined from the periodic table

*Step 3:* We generate the chemical and structural features for each graphlet in the three sets constructed in step 2. The basis of chemical features is 10 elemental properties listed in Table S1. Since a first-order graphlet is simply an atomic site, each elemental feature for the site is calculated as the weighted average of all constituents according to their occupancies. A second-order graphlet is a pair of neighboring sites, and we assign both chemical features and a single structural feature – the intra-pair distance. The calculation of the pair distance is straightforward, but chemical features of the pair should come from permutation-invariant combinations of the same features of the two sites. Most naturally, for each elemental property, we take the mean and the absolute difference of the site features to be the two features of the pair. The features of each site are still averaged over all constituent species, as in the first-order graphlets. A third-order graphlet consists of a triangle formed by three sites. It involves three pairwise distances and three angles, and the structural features should also be permutation-invariant combinations of the distances and angles. For both chemical and structural features, we take the mean, standard deviation (std), and kurtosis (kurt) as the three features for the triangle. At the end, we have 10 features for first-order graphlets (elemental features listed in Table S1), 21 features for second-order graphlets (mean and difference of the 10 elemental features plus one pair distance), and 36 features for third-order graphlets (mean, standard deviation, and kurtosis of the 10 elemental features, angles, and pair distances). The three graphlet sets and the corresponding features form the graphlet expansion of the materials.

*Step 4:* We convert the graphlet expansions of all materials into machine-readable histograms. A typical constraint in ML models is that inputs must be uniform in size and structure across all data points. Due to variations in crystal structures, materials generally have different numbers of graphlets. However, all materials are expanded to graphlet sets of three orders, and graphlets at the same order share the same set of features. Thus, we define features of a material at the graphlet set level, where each feature is actually a distribution of the corresponding feature of all graphlets at a specific order. These distributions can be naturally expressed in histogram format  $h = \{(m^{(1)}, h^{(1)}), (m^{(2)}, h^{(2)}), \dots, (m^{(n)}, h^{(n)})\}$ , with  $h^{(i)}$  being the count of the feature values from the graphlets at given order that fall into the *i*th bin that centers at  $m^{(i)}$ , as illustrated in Fig. S1 again. In our method, each material has 10 histograms from the first-order graphlet set, 21 histograms from the second-order graphlet set, and 36 histograms from the third-order graphlet set. All histograms should share the same number of bins, which is set

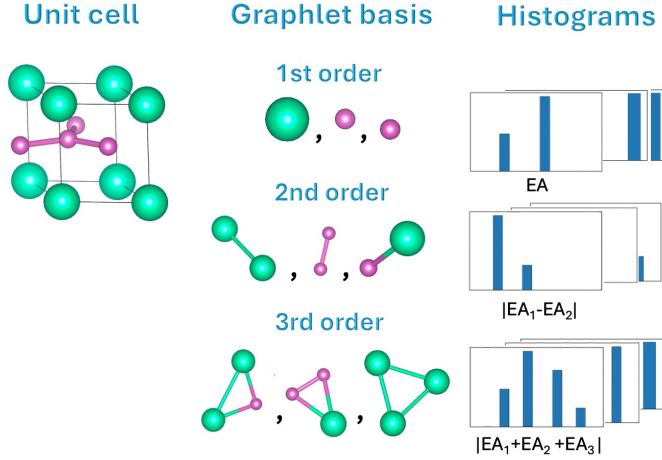


FIG. S1. Illustration of the complete graphlet basis to the third order and their histogram features generated from a primitive unit cell. The graphlet construction is based on the atomic sites instead of the elements. For example, two different atomic sites with the same element (purple) are considered inequivalent first-order graphlets. The histogram features come from permutation invariant combinations of the chemical features from different sites of the graphlets.

to be 20 in this work. For a particular feature, the histograms of different materials should have the same bin range, which is set by the minimum and maximum values of the corresponding graphlet feature among all graphlets of all materials in the dataset.

*Step 5:* To ensure consistency and comparability across different histogram features, we apply a standardization procedure to the bin midpoints of each histogram type. For each histogram feature, we compute the weighted mean and standard deviation of its bin midpoints across all materials in the dataset. The weights are given by the corresponding bin counts, which reflect the contribution of each bin. Let  $\{m^{(i)}\}$  denote the bin midpoints and  $\{h^{(i)}\}$  the corresponding counts aggregated over all samples for the histogram feature, as above. The weighted mean  $\bar{m}$  and standard deviation  $\sigma$  are computed as

$$\bar{m} = \frac{\sum_i m^{(i)} c^{(i)}}{\sum_i c^{(i)}}, \quad \sigma = \sqrt{\frac{\sum_i m^{(i)2} c^{(i)}}{\sum_i c^{(i)}} - (\bar{m})^2}. \quad (\text{S1})$$

Each bin midpoint  $m^{(i)}$  is then standardized as

$$m_s^{(i)} = \frac{m^{(i)} - \bar{m}}{\sigma}, \quad (\text{S2})$$

while the bin count  $h^{(i)}$  remains unchanged. This standardization is applied independently to each of the 67 histogram features, resulting in midpoints that are centered and scaled feature-wise. This normalization is particularly important for histogram-based kernel computations, such as the additive EMD kernel introduced in the GP section, which are sensitive to the scale of the feature space.

#### D. Symmetry features

Crystallographic symmetry plays an essential role in determining material properties. However, its treatment in machine learning applications for condensed matter physics remains at an early stage. On the feature level, some previous ML studies simply encode symmetry by supplying the space group number as an input. However, the space group number is a human-defined label and provides no intrinsic physical meaning to the model. On the modeling side, there has been growing interest in developing equivariant neural networks [43, 44], which ensure that model outputs transform appropriately under symmetry operations applied to the inputs. While such networks faithfully respect all symmetry operations of a given group (e.g., the Euclidean group), they are inherently agnostic to which specific symmetry elements are relevant to the target property and thus cannot learn to distinguish symmetry–property relationships.

In this work, we approach the problem from the perspective of feature design and introduce a principled method for encoding crystal symmetry into physically meaningful features. The symmetry of a crystalline material is described

by its space group. Since space groups are infinite (due to lattice translations), directly converting them into finite-dimensional features is challenging. Conveniently, space group operations can be represented as matrix-column pairs  $(\mathbf{W}, \mathbf{w})$ , where a point  $\mathbf{x}$  is mapped to  $\mathbf{W}\mathbf{x} + \mathbf{w}$ . The set of all linear parts  $\mathbf{W}$  from the symmetry operations of a space group  $\mathcal{G}$  forms its corresponding point group  $\mathcal{P}$  [45]. In three dimensions, there are only 32 crystallographic point groups, all of which are finite. One plausible approach is to design finite-dimensional symmetry indicators for space groups based on their point groups. However, this coarse-graining comes at a cost: many different space groups share the same point group and would thus be assigned identical indicators, leading to significant information loss.

To address the symmetry featurization in a more material-informative manner, we note that for different materials sharing the same space group, the occupations of Wyckoff positions in their unit cells can be different. Thus, it is necessary to reflect this degree of freedom in the features. To achieve this, for each material, we decided to examine the occupied sites in the unit cell and assign symmetry indicators based on their site-symmetry groups. The subgroup  $S_{\mathbf{x}}$  of symmetry operations from the space group  $\mathcal{G}$  of the material that fixes a crystal site  $\mathbf{x}$  is called the site-symmetry group of  $\mathbf{x}$  [45]. The site-symmetry group of an arbitrary crystal site in a material is isomorphic to a subgroup of the point group  $\mathcal{P}$  of the material's space group  $\mathcal{G}$ , which means a site-symmetry group in 3D is always isomorphic to a crystallographic point group. This allows us to first design symmetry indicators for each of the 32 crystallographic point groups and then generalize them to represent the site symmetry.

Following the Schoenflies notation, there are 11 distinct types of point group symmetry operations (excluding the identity), as summarized in Table S2. It is, therefore, natural to design the symmetry indicators as 11-dimensional vectors, where each dimension corresponds to one of these symmetry operation types. Then, for a given point group  $\mathcal{P}$ , we define the value of each feature dimension as the number of associated geometric elements—such as inversion centers, mirror planes, or rotation axes—that generate the corresponding symmetry operation. We choose to count geometric elements rather than symmetry operations because, for example, a single  $C_4$  axis generates three symmetry operations, whereas a single  $C_2$  axis generates only one. If we directly apply the number of symmetry operations, the value, while rigorous and straightforward from the maths perspective, may introduce bias to the ML model. In Table S3, we list the values of all symmetry feature dimensions for the 32 crystallographic point groups, where each row represents the 11-dimensional symmetry vector corresponding to one point group (see Fig. S2).

TABLE S2. The 11 types of point group symmetry operations (excluding identity), following the Schoenflies notation.

Symbol	Name	Description
$i$	Inversion	Inversion through the origin: $\vec{r} \rightarrow -\vec{r}$
$\sigma_v$	Vertical mirror plane	Mirror plane parallel to the principal rotation axis
$\sigma_h$	Horizontal mirror plane	Mirror plane perpendicular to the principal rotation axis
$\sigma_d$	Dihedral mirror plane	Mirror plane at diagonal angles between vertical planes
$C_2$	Two-fold rotation	Rotation by $180^\circ$ about the principal axis
$C_3$	Three-fold rotation	Rotation by $120^\circ$ about the principal axis
$C_4$	Four-fold rotation	Rotation by $90^\circ$ about the principal axis
$C_6$	Six-fold rotation	Rotation by $60^\circ$ about the principal axis
$\bar{3}$	Three-fold improper rotation	$C_3$ rotation followed by reflection through perpendicular plane
$\bar{4}$	Four-fold improper rotation	$C_4$ rotation followed by reflection through perpendicular plane
$\bar{6}$	Six-fold improper rotation	$C_6$ rotation followed by reflection through perpendicular plane

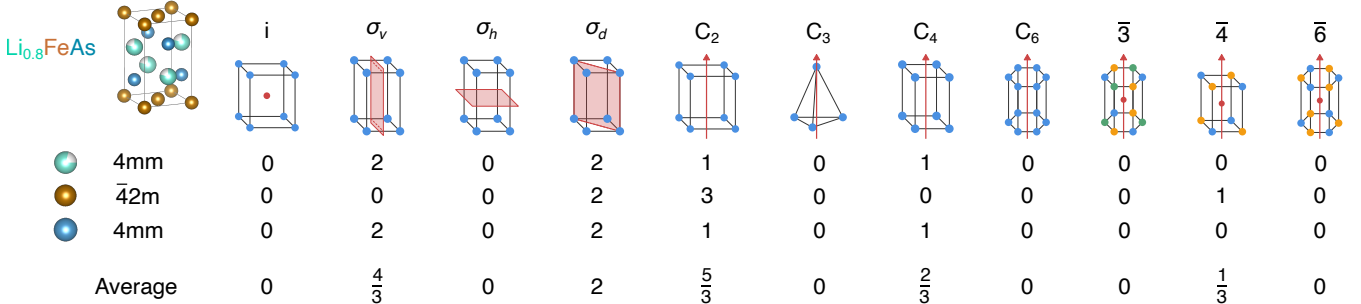


FIG. S2. The eleven point group operations assigned to each site by its crystallographic point group. The crystal symmetry vector is obtained by averaging site symmetry vectors over all inequivalent occupied sites in the unit cell.

After constructing symmetry indicators for the 32 crystallographic point groups, we apply a consistent procedure to generate the symmetry feature for each CIF file. Our implementation is based on two Python li-

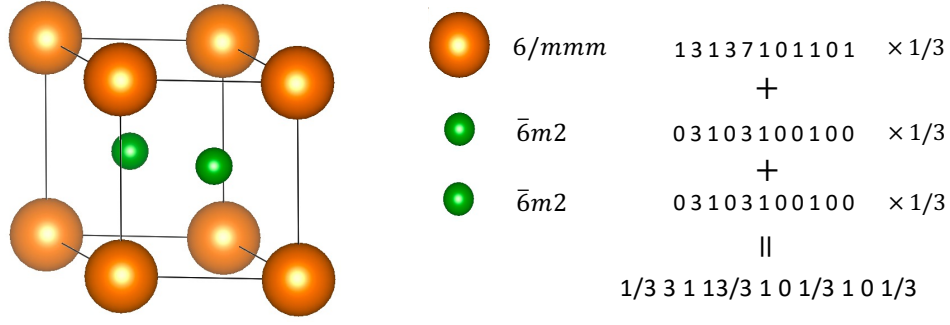


FIG. S3. Illustration of obtaining the symmetry feature of  $\text{MgB}_2$ . The point group isomorphic to the site-symmetry group of the Mg site is  $6/mmm$ , and the point group isomorphic to the site-symmetry group of the two B sites is  $\bar{6}m2$ . Their corresponding 11-dimensional symmetry indicators are listed in Table S3. The symmetry feature of the material is the dimension-wise average of the three 11-dimensional vectors.

braries, `pymatgen` and `spglib`. First, we identify all inequivalent atomic sites within the unit cell. Then, using `SpaceGroupAnalyzer.get_symmetry_operations()` from `pymatgen`, we obtain the truncated set of symmetry operations that is sufficient for site-symmetry group determination. After getting the set, for each occupied site in the unit cell, we iterate through the operations  $(\mathbf{W}, \mathbf{w})$  in this set and retain those satisfying  $\mathbf{W}\mathbf{x} + \mathbf{w} \equiv \mathbf{x}$ , i.e., those that leave the site  $\mathbf{x}$  invariant. The rotation components  $\mathbf{W}$  of these operations are then passed to `spglib.get_pointgroup()`, which returns the corresponding crystallographic point group. Once the associated point groups of all inequivalent atomic sites are identified, their 11-dimensional symmetry indicators are retrieved. The final symmetry feature vector for the material is obtained by computing the dimension-wise average over the indicators of all inequivalent sites. The procedure is illustrated in Fig. S2 for  $\text{Li}_{0.8}\text{FeAs}$ , and another example,  $\text{MgB}_2$ , is shown in Fig. S3.

TABLE S3. Symmetry feature vectors for the 32 crystallographic point groups. Each row corresponds to one point group and is essentially an 11-dimensional symmetry vector, with each column indicating the number of associated geometric elements for the corresponding symmetry operation type.

Point Group	$i$	$\sigma_v$	$\sigma_h$	$\sigma_d$	$C_2$	$C_3$	$C_4$	$C_6$	3	4	6
1	0	0	0	0	0	0	0	0	0	0	0
$\bar{1}$	1	0	0	0	0	0	0	0	0	0	0
2	0	0	0	0	1	0	0	0	0	0	0
$m$	0	0	1	0	0	0	0	0	0	0	0
$2/m$	1	0	1	0	1	0	0	0	0	0	0
222	0	0	0	0	3	0	0	0	0	0	0
$mm2$	0	2	0	0	1	0	0	0	0	0	0
$mmm$	1	2	1	0	3	0	0	0	0	0	0
4	0	0	0	0	1	0	1	0	0	0	0
$\bar{4}$	0	0	0	0	1	0	0	0	0	1	0
$4/m$	1	0	1	0	1	0	1	0	0	1	0
422	0	0	0	0	5	0	1	0	0	0	0
$4mm$	0	2	0	2	1	0	1	0	0	0	0
$\bar{4}2m$	0	0	0	2	3	0	0	0	0	1	0
$4/mmm$	1	2	1	2	5	0	1	0	0	1	0
3	0	0	0	0	0	1	0	0	0	0	0
$\bar{3}$	1	0	0	0	0	1	0	0	0	0	1
32	0	0	0	0	3	1	0	0	0	0	0
$3m$	0	3	0	0	0	1	0	0	0	0	0
$\bar{3}m$	1	0	0	3	3	1	0	0	0	0	1
6	0	0	0	0	1	1	0	1	0	0	0
$\bar{6}$	0	0	1	0	0	1	0	0	1	0	0
$6/m$	1	0	1	0	1	1	0	1	1	0	1
622	0	0	0	0	7	1	0	1	0	0	0
$6mm$	0	3	0	3	1	1	0	1	0	0	0
$\bar{6}m2$	0	3	1	0	3	1	0	0	1	0	0
$6/mmm$	1	3	1	3	7	1	0	1	1	0	1
23	0	0	0	0	3	4	0	0	0	0	0
$m\bar{3}$	1	0	3	0	3	4	0	0	0	0	4
432	0	0	0	0	9	4	3	0	0	0	0
$\bar{4}3m$	0	0	0	6	3	4	0	0	0	3	0
$m\bar{3}m$	1	0	3	6	9	4	3	0	0	3	4

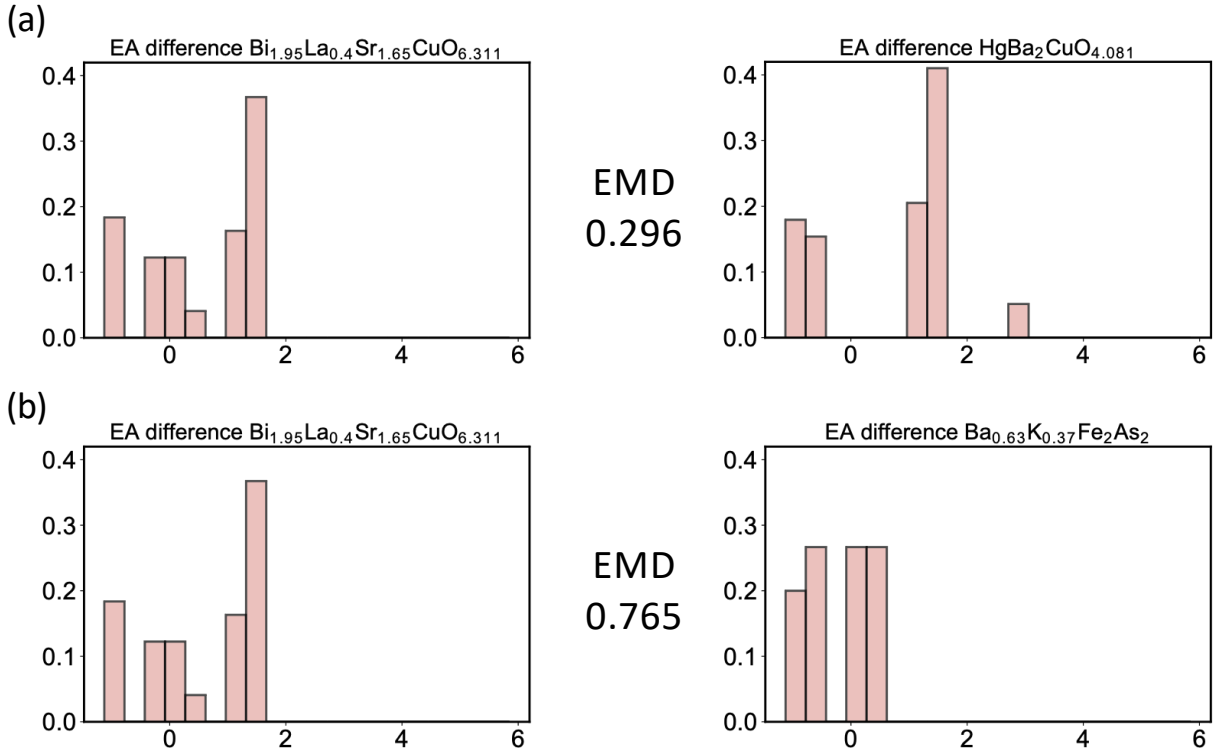


FIG. S4. Examples of the EMDs between two pairs of materials. Panel (a) shows the EMD between histograms of second-order EA difference from two cuprate materials. The chemical properties of materials from the same class are similar, and the EMD value is small. (b) shows the EMD between histograms of second-order EA difference from a cuprate material and an iron-based material. The chemical properties of materials from different classes are different, and the EMD value is large.

## II. GAUSSIAN PROCESS BASED ON THE EMD KERNEL

For ML-based  $T_c$  prediction, we compare a flexible but opaque strategy using a neural network (NN) and a more transparent, probabilistic model using  $\text{GPT}_c$ , as illustrated in Fig. S5(a). In this work, we use Gaussian process (GP) models for two tasks: (i) regression to predict the superconducting critical temperature  $T_c$ , and (ii) binary classification of whether a material is a superconductor. To perform the two tasks, we build both GP regressors and GP classifiers. For both tasks, the input features are either graphlet features alone or graphlet features augmented with symmetry features. We model symmetry features with a standard automatic relevance determination (ARD) kernel. Graphlet features are represented as histograms and compared via the earth mover’s distance (EMD); accordingly, we construct an EMD-based kernel over the histograms. Below, we first introduce EMD and the resulting EMD kernel, and then briefly describe the GP regressors and classifiers.

The symmetry indicators, which are scalar features, are modeled using the standard RBF kernel, and the final kernel over all features is a product of this RBF kernel with the EMD histogram kernel. We note that the length scales for the EMD and RBF kernels are normalized differently: for histograms, the bin centers are standardized, whereas for symmetry features, the values themselves are standardized to be within  $[0, 1]$ . The GP combined with the EMD kernel provides a principled way to model histogram features, enabling analysis of each feature’s sensitivity while preserving its distributional structure.

### A. Earth mover’s distance

The earth mover’s distance (EMD) [15] is a metric that quantifies the dissimilarity between two distributions, which is used to analyze jets in particle collider experiments [16]. Mathematically, the EMD is a metric between two distributions,  $A = \{(\mathbf{a}_1, w_{\mathbf{a}_1}), \dots, (\mathbf{a}_n, w_{\mathbf{a}_n})\}$  and  $B = \{(\mathbf{b}_1, w_{\mathbf{b}_1}), \dots, (\mathbf{b}_m, w_{\mathbf{b}_m})\}$ , where  $\mathbf{a}_i, \mathbf{b}_i$  denote the positions of the clusters, and  $w_{\mathbf{a}_i}, w_{\mathbf{b}_i}$  denote the weights. For the general case where the weights of  $A$  and  $B$  are not

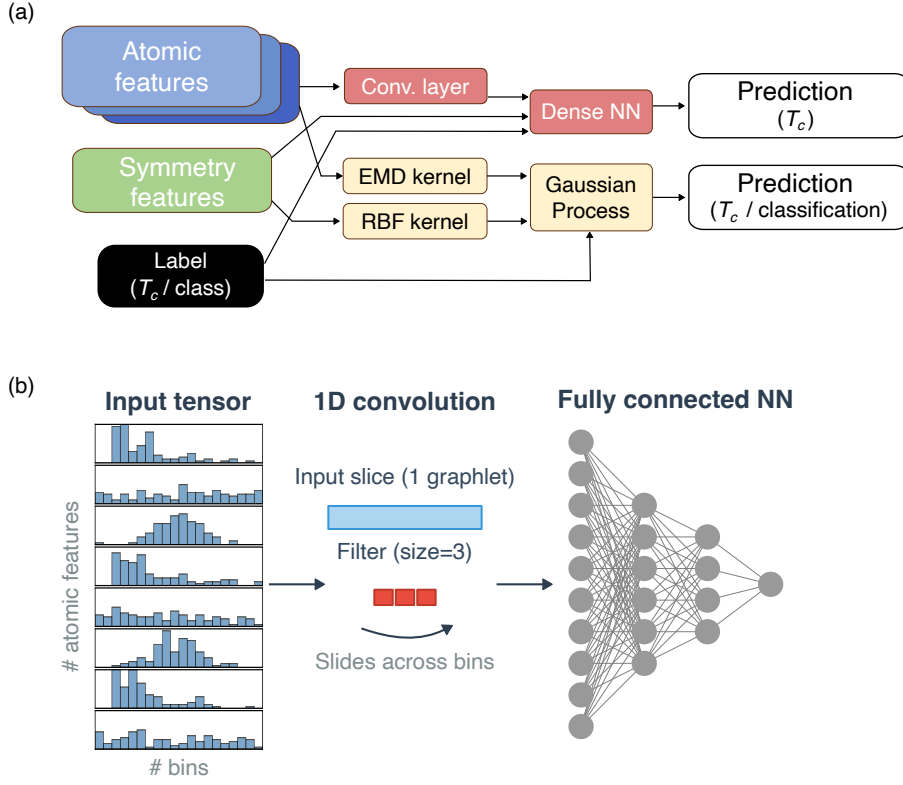


FIG. S5. (a) Flowchart describing the machine learning strategy in this work. We feed graphlet histograms and symmetry vectors into neural networks and GP models for the  $T_c$  prediction task, and into GP classifier for the SC classification task. (b) For the neural networks, the graphlet histograms go through a convolutional layer before being passed to a fully connected feed-forward NN.

normalized, and the numbers of clusters are different ( $n \neq m$ ), we look for a flow  $F = [f_{ij}]$ , where  $f_{ij}$  denotes the flow from  $\mathbf{a}_i$  to  $\mathbf{b}_j$ , that minimizes the work

$$\text{work}(A, B, F) = \sum_{ij} d_{ij} f_{ij}, \quad (\text{S3})$$

subject to the constraints:

$$f_{ij} \geq 0 \quad 1 \leq i \leq n, \quad 1 \leq j \leq m \quad (\text{S4})$$

$$\sum_j f_{ij} \leq w_{\mathbf{a}_i} \quad (\text{S5})$$

$$\sum_i f_{ij} \leq w_{\mathbf{b}_j} \quad (\text{S6})$$

$$\sum_{ij} f_{ij} = \min\left(\sum_i w_{\mathbf{a}_i}, \sum_j w_{\mathbf{b}_j}\right), \quad (\text{S7})$$

where  $d_{ij} = |\mathbf{a}_i - \mathbf{b}_j|$ . Intuitively, think of  $A$  as piles of sand and  $B$  as holes; the constraints enforce that the amount of moved sand equals the smaller of the two total masses, so either all the sand is moved or all the holes are filled, whichever is smaller. After obtaining the optimal flow, the EMD is the minimal work normalized by the total flow

$$\text{EMD} = \frac{\sum_{ij} d_{ij} f_{ij}}{\sum_{ij} f_{ij}}, \quad (\text{S8})$$

where the total flow is also equal to the total weights of the smaller distribution.

Our graphlet features are discrete histograms  $h = \{(m^{(1)}, h^{(1)}), (m^{(2)}, h^{(2)}), \dots, (m^{(n)}, h^{(n)})\}$ , and each feature dimension shares equally spaced bin centers  $\{m^{(i)}\}$ . In order to forego the normalization factor in the denominator,

we normalize the weights of each histogram to have  $\sum h^{(i)} = 1$ . Then the EMD can be simply expressed as

$$\text{EMD}(h_1, h_2) = \min_F \left( \sum_{i=1}^n \sum_{j=1}^n d|i-j|f_{ij} \right), \quad (\text{S9})$$

where  $d = \Delta m = m^{(i)} - m^{(i-1)}$ . In Fig. S4, we show exemplary pairs of histogram features that have small and large EMD values.

Given that the EMD defines a meaningful distance between individual histograms, we construct an additive EMD kernel for two ‘‘vectors’’ of histograms,  $x_i = (h_{i1}, h_{i2}, \dots, h_{iq})$  and  $x_j = (h_{j1}, h_{j2}, \dots, h_{jq})$ , where  $q$  is the number of features (in our case,  $q = 21$  for second-order graphlet features, and  $q = 21 + 36 = 57$  when third-order graphlet features are additionally included). The additive EMD kernel takes the form

$$k_{\text{EMD}}(x_i, x_j) = \sum_{n=1}^q w_n \exp \left( -\frac{\text{EMD}(h_{in}, h_{jn})}{\ell_n} \right), \quad (\text{S10})$$

where  $w_n$  and  $\ell_n$  are learnable parameters. Since histogram features can have complicated shapes and there may exist few feature dimensions where most of the histograms look unsimilar (yielding large EMDs), the additive form aggregates per-dimension similarities so that high similarity on informative dimensions is not suppressed; this prevents the kernel from collapsing to small values due to a few ‘‘bad’’ dimensions (whereas a product across dimensions would be dominated by them). In actual implementations, the EMDs are calculated by the `wasserstein_1d` function in the Python Optimal Transport (POT) library [46].

When the input includes only graphlet features, both the GP regressors and classifiers directly employ the additive EMD kernel. When the input includes both graphlet features and symmetry features, the models employ the product of the additive EMD kernel and a standard ARD kernel:  $k = \sigma^2 k_{\text{EMD}} \cdot k_{\text{ARD}}$ . This multiplicative coupling yields high covariance only when the inputs are similar in *both* feature spaces; dissimilarity in either space down-weights the covariance, thereby encouraging the model to leverage information from both graphlet and symmetry features.

## B. Proof that the EMD kernel is a valid kernel

For successful GP-based learning with our unique histogram features, we need to construct a suitable and valid kernel based on a meaningful metric in the feature space. The EMD already used to navigate the multiplicity of CIFs will be a natural metric. However, constructing a valid Mercer kernel from the EMD is nontrivial. General EMD in  $d$  dimensions is nonlinear, and transformations that are commonly done in machine learning to more common Euclidean distance metrics (like  $\psi(r) := \exp(-r^2)$ ) do not necessarily work, because the EMD Gram matrix is not conditionally negative definite. For instance, while it is tempting to construct a kernel that mimics more popular kernels, such as the radial basis function (RBF) kernel, e.g., by squaring the EMD, this does not result in a valid kernel.

As defined in Eq. (S9), the EMD with an L1 ground metric is given by

$$\text{EMD}(h_1, h_2) = \min_F \left( d \sum_{i,j} |i-j| f_{ij} \right).$$

Let  $C(h) \in \mathbb{R}^n$  be the cumulative histogram of  $h$ :

$$[C(h)]_k \triangleq \sum_{b=1}^k h_b,$$

where  $[C(h)]_k$  denotes the  $k$ th bin of the cumulative histogram. A well known property of the 1D EMD with L1 ground distance is a reduction to an L1 distance (see e.g. Ref. [47]):

$$\text{EMD}(h_1, h_2) = d \|C(h_1) - C(h_2)\|_1, \quad (\text{S11})$$

where again  $d$  is the distance between bin centers. Because the L1 distance  $\|u - v\|_1$  is conditionally negative definite, by Schoenberg’s theorem, the function

$$k_t(u, v) = \exp(-\ell_n \|u - v\|_1)$$

is positive definite for any  $\ell_n > 0$ . Therefore

$$k(h_1, h_2) := \exp(-\ell_n \|C(h_1) - C(h_2)\|_1) = \exp\left(-\frac{\text{EMD}(h_1, h_2)}{\ell_n}\right) \quad (\text{S12})$$

is positive definite (PD). This demonstrates that the kernel restricted to any single pair of histograms is valid. Finally, non-negative weighted sums of PD kernels are PD (since  $v^\top [\sum w_i K_i] v = \sum w_i v^\top K_i v > 0$ ). Therefore, the final kernel expression,

$$K_{\text{EMD}}(x_i, x_j) = \sum_n w_n \exp\left(-\frac{\text{EMD}(h_{i,n}, h_{j,n})}{\ell_n}\right), \quad (\text{S13})$$

is positive definite because it is a positively weighted sum of the ‘‘individual histogram EMD’’ kernel that we just proved is a valid kernel.

### C. Details of the GP

Once we constructed the appropriate kernel for the features, the GP regressors follow the standard exact Gaussian process regression formulation. Given training data  $\mathcal{D} = \{(x_i, y_i)\}_{i=1}^N$  with inputs  $x_i$  including graphlet features/graphlet+symmetry features and target  $y_i = T_{c,i}$ , we place a GP prior on a latent function  $f$ :

$$f \sim \mathcal{GP}(m(\cdot), k(\cdot, \cdot; \theta)), \quad (\text{S14})$$

where  $m(\cdot)$  is the mean function and  $k(\cdot, \cdot; \theta)$  is the covariance. In our setup,  $k$  is either the EMD kernel  $k_{\text{EMD}}$  (graphlet-only) or the product kernel  $k = \sigma^2 k_{\text{EMD}} \cdot k_{\text{ARD}}$  (graphlet + symmetry).

Observations follow a Gaussian noise model:

$$y_i = f(x_i) + \varepsilon_i, \quad \varepsilon_i \sim \mathcal{N}(0, \sigma_n^2). \quad (\text{S15})$$

Let  $X = [x_1, \dots, x_N]$ ,  $\mathbf{y} = [y_1, \dots, y_N]^\top$ ,  $\mathbf{m}_X = [m(x_1), \dots, m(x_N)]^\top$ ,  $K_{XX} = [k(x_i, x_j)]_{i,j}$ , and  $K_y = K_{XX} + \sigma_n^2 I$ . For a test input  $x_\star$ , define  $\mathbf{k}_\star = [k(x_1, x_\star), \dots, k(x_N, x_\star)]^\top$ . The exact GP posterior over the latent  $f(x_\star)$  is Gaussian with mean and variance

$$\mu_\star = m(x_\star) + \mathbf{k}_\star^\top K_y^{-1} (\mathbf{y} - \mathbf{m}_X), \quad (\text{S16})$$

$$v_\star = k(x_\star, x_\star) - \mathbf{k}_\star^\top K_y^{-1} \mathbf{k}_\star. \quad (\text{S17})$$

The predictive distribution for a noisy observation adds the noise variance:

$$\text{Var}(y_\star) = v_\star + \sigma_n^2. \quad (\text{S18})$$

The kernel hyperparameters  $\theta$  (e.g.,  $\{w_n, \ell_n\}_{n=1}^d$  in  $k_{\text{EMD}}$ , any amplitude  $\sigma^2$ , the noise  $\sigma_n^2$ , and mean parameters) are learned by maximizing the log marginal likelihood:

$$\log p(\mathbf{y} | X, \theta) = -\frac{1}{2} (\mathbf{y} - \mathbf{m}_X)^\top K_y^{-1} (\mathbf{y} - \mathbf{m}_X) - \frac{1}{2} \log |K_y| - \frac{N}{2} \log(2\pi). \quad (\text{S19})$$

Gradients of this objective with respect to  $\theta$  are computed analytically and used in standard gradient-based optimization.

Finally, we briefly introduce the variational GP classifier for binary labels  $y_i \in \{-1, +1\}$ . We also start with positing a latent function  $f$  with GP prior described in Eq. (11). To obtain a tractable approximation under the non-Gaussian classification likelihood, we introduce inducing inputs  $\mathbf{Z} = [z_1, \dots, z_M]$  and the corresponding inducing variables  $\mathbf{u} = f(\mathbf{Z})$  with prior

$$p(\mathbf{u}) = \mathcal{N}(\mathbf{m}_Z, K_{ZZ}), \quad \mathbf{m}_Z = [m(z_1), \dots, m(z_M)]^\top, \quad K_{ZZ} = [k(z_i, z_j)]_{i,j}. \quad (\text{S20})$$

In our setting we take  $\mathbf{Z} = \mathbf{X}$  (i.e.,  $M = N$ ), so inducing variables are used as a variational device rather than for sparsification. Then, we approximate the analytically intractable posterior by a Gaussian variational posterior over  $\mathbf{u}$ ,

$$q(\mathbf{u}) = \mathcal{N}(\boldsymbol{\mu}_u, \mathbf{S}_u), \quad (\text{S21})$$

which induces the approximate posterior process

$$q(f(\cdot)) = \int p(f(\cdot) | \mathbf{u}) q(\mathbf{u}) d\mathbf{u}. \quad (\text{S22})$$

For a test input  $x_*$ , define  $\mathbf{k}_{Z_*} = [k(z_1, x_*), \dots, k(z_M, x_*)]^\top$  and  $k_{**} = k(x_*, x_*)$ . The resulting predictive marginal over the latent  $f(x_*)$  is Gaussian,

$$q(f(x_*)) = \mathcal{N}(\mu_*, v_*), \quad (\text{S23})$$

with

$$\mu_* = m(x_*) + \mathbf{k}_{Z_*}^\top K_{ZZ}^{-1} (\boldsymbol{\mu}_u - \mathbf{m}_Z), \quad (\text{S24})$$

$$v_* = k_{**} + \mathbf{k}_{Z_*}^\top K_{ZZ}^{-1} (\mathbf{S}_u - K_{ZZ}) K_{ZZ}^{-1} \mathbf{k}_{Z_*}. \quad (\text{S25})$$

For the probit likelihood, we model

$$p(y_i | f(x_i)) = \Phi(y_i f(x_i)), \quad (\text{S26})$$

where  $\Phi(\cdot)$  is the standard normal CDF. The kernel hyperparameters  $\theta$  and the variational parameters  $(\boldsymbol{\mu}_u, \mathbf{S}_u)$  are learned by maximizing the evidence lower bound (ELBO):

$$\mathcal{L}_{\text{ELBO}} = \sum_{i=1}^N \mathbb{E}_{q(f(x_i))} [\log \Phi(y_i f(x_i))] - \text{KL}[q(\mathbf{u}) \| p(\mathbf{u})]. \quad (\text{S27})$$

At prediction time, the class probability is obtained by integrating the probit link against  $q(f(x_*))$ ; using the probit–Gaussian identity,

$$p(y_* = 1 | x_*) = \int \Phi(f) \mathcal{N}(f | \mu_*, v_*) df = \Phi\left(\frac{\mu_*}{\sqrt{1 + v_*}}\right). \quad (\text{S28})$$

### III. NEURAL NETWORKS

While GP is interpretable, its expressiveness can be limited. We therefore explore learning from our data using modern neural networks, which are known to be highly expressive, albeit not interpretable.

The proposed neural network is specifically designed to process and classify histogram-like data, where individual features are represented as distributions across discrete bins. The architecture leverages a combination of convolutional and fully connected layers to extract meaningful relationships both within and across multiple histogram representations. Initially, a convolutional module processes the bin-wise data for each feature independently, employing a 1D convolutional layer with a kernel size of 3 and padding of 1, paired with batch normalization and ReLU activation. We use  $N_F = 64$  convolutional filters. This configuration is suitable for histograms as it captures local relationships between adjacent bins (e.g., trends or smooth transitions in the distribution), while batch normalization ensures stable training dynamics. Furthermore, the network explicitly incorporates the weighted contribution of bin centers and counts, encoding additional spatial information about the histogram beyond the raw bin heights.

The outputs of the convolutional module are flattened into a single feature vector, combining all histogram properties. Each histogram is represented by a vector of dimension  $N_F = 64$ , leading to an overall feature vector of size  $N_F \times N_{\text{histograms}}$ . Fully connected layers are then used to transform this high-dimensional representation into lower-dimensional feature embeddings, facilitating global interactions across all input properties. We use two fully connected layers, the first one with 150 neurons and the second with 32 neurons. For the classification task (SC vs. non-SC), the network concludes with a sigmoid activation function, producing a probability score suitable for binary classification. For the  $T_c$  prediction task, the last output is not passed through a sigmoid, since it should return a continuous number. This process is illustrated in Fig. S5(b).

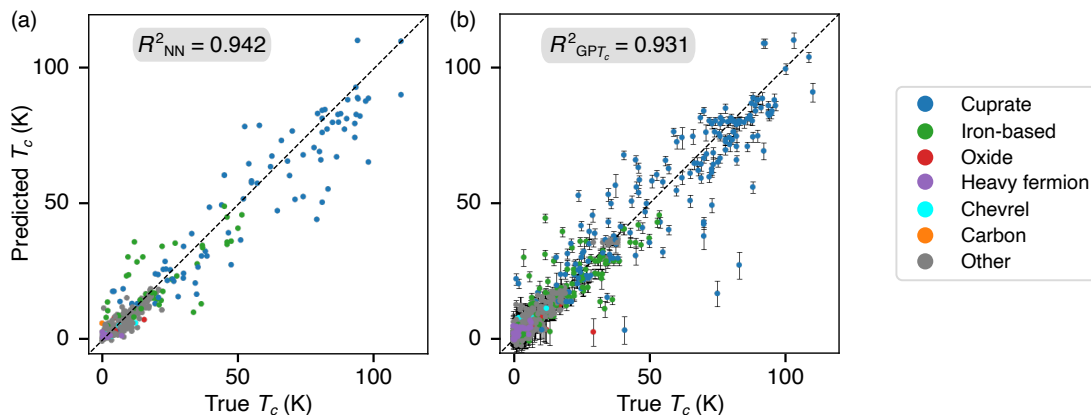


FIG. S6. Performance comparison in  $T_c$  prediction of (a) the neural network and (b) the Gaussian process,  $\text{GPT}_c$ . The models are almost on par.

#### IV. PERFORMANCE COMPARISON

Figure S6 shows that the performance of our GP model,  $\text{GPT}_c$ , is very close to that of the neural network. While the NN yields  $R^2 = 0.942$ ,  $\text{GPT}_c$  gets to  $R^2 = 0.931$  which is very close, while being interpretable.

An unexpected outcome was the little significance the symmetry features carried in determining  $T_c$  (see the feature ranking in Sec. V.A). To gain insight into this, we trained a model with four of the best histogram features and all 11 symmetry features. We show the resulting GP length scales ( $\ell_n$  in Eq. (1) of the main text) associated with the 11 symmetry features in Fig. S7(a). Notice that the absolute scale of the length scale  $\ell$  for the graphlet features and the histogram features are different as they enter two separate kernels. Inspecting the actual distribution of the symmetry features, more predictive symmetry features ( $\sigma_d$  and  $C_4$ ) exhibit distinct distributions that correlate with  $T_c$  trends. On the other hand, the two least predictive features either show a broad, uninformative spread with  $T_c$  ( $i$ ) or display almost no variation with  $T_c$  at all ( $C_6$ ); see Fig. S7(b). All in all, given that the  $T_c$  prediction task was based on superconducting materials, the fact that most of the materials share similar symmetry removed predictive power from symmetry features when it came to predicting  $T_c$  among superconductors. The symmetry features, however, are more predictive of whether a material will superconduct.

#### V. IDENTIFYING SIGNIFICANT FEATURES

##### A. $T_c$ prediction

Our GP regression results [Fig. 3(d) of the main text] show that the significant boost in performance comes from including second-order histogram features, i.e., going beyond simple averages. Adding third-order histogram features provides only a modest improvement on top of that. In light of this, and in order to reduce the combinatorial space, we limit our feature removal experiments to second-order histogram features + symmetry features.

Our feature removal experiment proceeds as follows. We start from the full set of  $N = 32$  features (21 second-order histogram features + 11 symmetry features), and train a  $T_c$  prediction GP model. We then train  $N$  different GP models, where each time a different one of the  $N$  features is removed, so only the remaining  $N - 1$  features participate in the regression. For each model, we evaluate the performance using the  $R^2$  score on the test set. Identifying the model with the highest test  $R^2$  score singles out the least predictive feature: the one that has been removed in that particular model. This leaves us with a set of  $N - 1$  features, that are the most predictive subset of the original set of  $N$  features.

We then proceed iteratively: starting from  $N - 1$  features that were most predictive in the previous iteration, we train  $N - 1$  models (each with a different one of the  $N - 1$  features is removed), and find the model with the highest test  $R^2$  score. This allows us to remove an additional feature, leaving us with  $N - 2$  features. This process repeats iteratively all the way to keeping just one feature. We track the performance (test  $R^2$  score) of the best models along this feature removal process in Fig. 3(e) of the main text. We find that the best overall model yields  $R_{\text{opt}}^2 = 0.933$ , and keeping just four features yields  $R_4^2 = 0.922$ , which is quite close to  $R_{\text{opt}}^2$  (for reference, the most predictive single feature gives  $R_1^2 = 0.864$ ). It is also apparent from Fig. 3(e) of the main text that the curve starts to flatten around

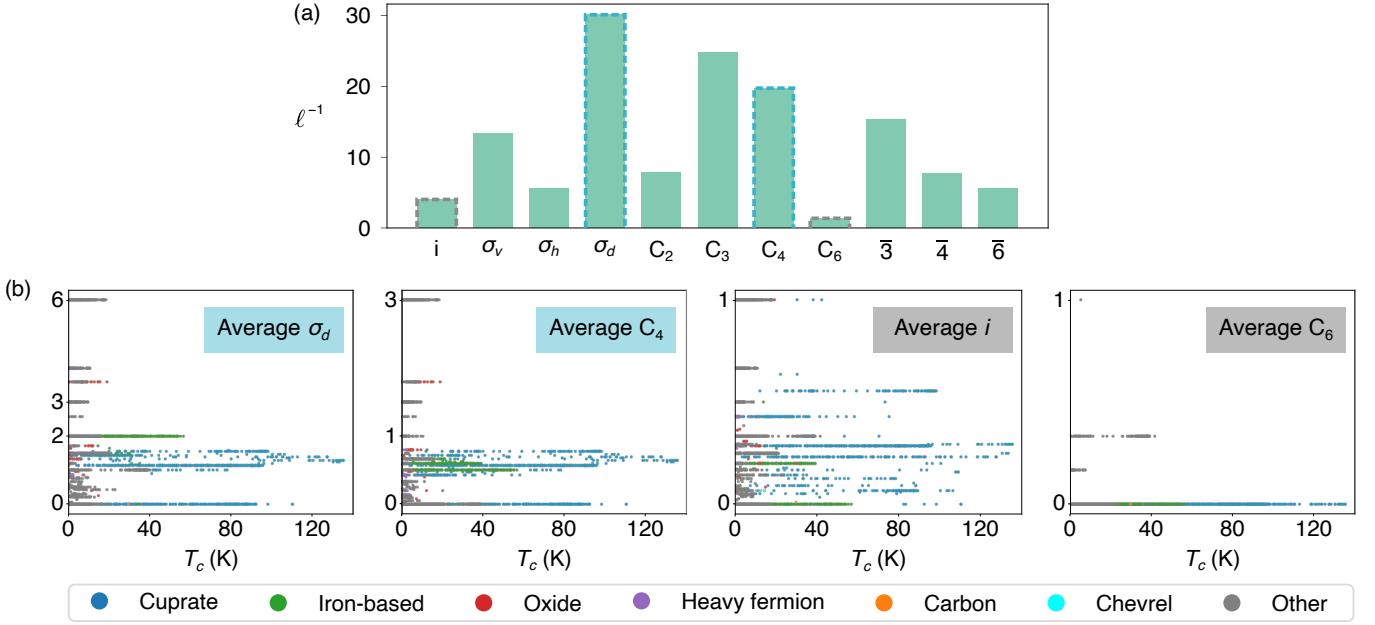


FIG. S7. (a) Inverse length scales of the 11 symmetry features, in  $T_c$  prediction. (b)  $T_c$  vs. four exemplary average symmetry features. In the left plots,  $\sigma_d$  and  $C_4$  [shown as dashed blue lines in (a)], which are learned as highly predictive by the GP, show distinct shapes that partly differentiate between values of  $T_c$ . In the right plots,  $i$  and  $C_6$  [shown as dashed gray lines in (a)], which are learned as not predictive by the GP, exhibit either a large spread in  $T_c$  ( $i$ ) or almost no change in  $T_c$  ( $C_6$ ).

four features, with the additional improvements from including extra features getting smaller and smaller.

We list here the features by the predictiveness according to the feature removal analysis, sorted from the most predictive one to the least predictive one:

1. Electron affinity difference
2. Inter-atomic distance
3. Total number of valence electrons mean
4. Column in the periodic table mean
5. Number of d valence electrons mean
6. Number of p valence electrons mean
7. Atomic weight mean
8. Number of s valence electrons mean
9. Vertical mirror plane
10. 6-fold rotation axis
11. Pauling electronegativity mean
12. 6-fold rotoinversion axis
13. Covalent radius difference
14. 4-fold rotoinversion axis
15. Number of d valence electrons difference
16. Total number of valence electrons difference
17. 4-fold rotation axis

18. 3-fold rotation axis
19. Ionization potential mean
20. Dihedral mirror plane
21. 3-fold rotoinversion axis
22. Number of p valence electrons difference
23. Number of s valence electrons difference
24. Pauling electronegativity difference
25. Covalent radius mean
26. Column in the periodic table difference
27. Horizontal mirror plane
28. Atomic weight difference
29. Ionization potential difference
30. Inversion center
31. 2-fold rotation axis
32. Electron affinity mean

This finding motivated us to examine all possible combinations of four features: the combinatorial space is  $\binom{32}{4} = 35,960$ , which is large but reasonable. See the database for the outcome of the combinatorial search.

## B. Classification

Following the same feature pruning procedure we used for  $T_c$  prediction, we train GP models to identify the most predictive features for SC / non-SC classification. The features are listed here in order from the most predictive one to the least predictive one for classification:

1. Number of d valence electrons difference
2. Ionization potential mean
3. Atomic weight mean
4. Dihedral mirror plane
5. 3-fold rotation axis
6. Total number of valence electrons difference
7. Number of s valence electrons mean
8. Electron affinity difference
9. Number of p valence electrons difference
10. Number of p valence electrons mean
11. Atomic weight difference
12. Inversion center
13. Pauling electronegativity mean
14. Covalent radius difference

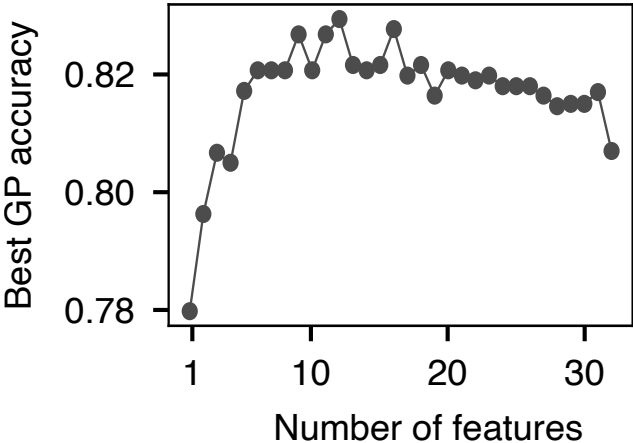


FIG. S8. Performance of the GP classifier when only subsets of features are included. The model’s performance begins to degrade when the number of features falls below 10.

- 15. Number of s valence electrons difference
- 16. Total number of valence electrons mean
- 17. Column in the periodic table difference
- 18. Column in the periodic table mean
- 19. Inter-atomic distance
- 20. 4-fold rotation axis
- 21. Vertical mirror plane
- 22. 3-fold rotoinversion axis
- 23. 6-fold rotation axis
- 24. Ionization potential difference
- 25. Number of d valence electrons mean
- 26. Horizontal mirror plane
- 27. 4-fold rotoinversion axis
- 28. Covalent radius mean
- 29. 2-fold rotation axis
- 30. Pauling electronegativity difference
- 31. 6-fold rotoinversion axis
- 32. Electron affinity mean

The feature-pruning experiment on the classifier shows that more histogram features are necessary for classifier predictions. Specifically, Fig. S8 shows that achieving full performance requires approximately 10 histogram features (see Sec. V.B). Atomic weight mean and EA difference stand out as predictive for both classification and  $T_c$  regression, and apart from them the predictive features for the two tasks have little overlap, with the symmetry features being much more predictive for classification than for regression (see Sec. V). Our observation that features predicting whether a material superconducts are distinct from the features predicting  $T_c$  is in line with the observations in an early manual statistical analysis using elemental features [48].

## VI. FILTERING OF NEW PREDICTIONS

### A. Feature Construction and Prediction Pipeline for ICSD

To extend the model beyond the 3DSC dataset and evaluate superconductivity across the broader landscape of known inorganic materials, we generated graphlet and symmetry features for most entries in the ICSD. ICSD provides crystallographic data for more than 225,000 experimentally synthesized inorganic compounds, offering a comprehensive platform for large-scale screening. Using the featurization workflow described in the main text (and detailed in SM Sec. I–II), we processed all ICSD entries with machine-readable CIFs to generate graphlet features for approximately 185,000 materials.

Graphlet features were computed following the same protocol as we did with the materials within the 3DSC. First-, second-, and third-order graphlets were constructed to capture local chemical environments and structural motifs through distributions of elemental descriptors, interatomic distances, and bond angles (see Fig. 2(a) and SM Sec. I.C). For ICSD screening, we primarily relied on second-order graphlets together with symmetry features, since these were shown to retain the vast majority of predictive power while limiting model complexity. To ensure compatibility with the trained GP models, all ICSD histogram features were standardized using the same bin centers defined during 3DSC preprocessing. This alignment preserves a consistent feature space for EMD-based kernel comparisons.

Predictions from the GP classifier and  $GPT_c$  for each ICSD ID formed the starting point of our analysis.

### B. Post-processing and Filtering of ICSD Predictions

The full set of approximately 185,000 predictions was subsequently filtered to identify promising superconducting candidates and prioritize materials for follow-up analysis.

#### 1. $T_c > 10\text{ K}$

In this regime, the  $GPT_c$  exhibits relatively low uncertainty [Fig. 3(b–c) of the main text], making its output a reliable basis for screening. We focus on materials with

1. the predicted  $T_c > 10\text{ K}$ ,
2. classification probability  $> 0.5$ .

To focus on unexplored chemical space, we removed materials belonging to the well-established high- $T_c$  families: cuprates and iron-based superconductors.

#### 2. $2\text{ K} < T_c < 10\text{ K}$

There are many more predictions for  $T_c < 10\text{ K}$  though likely they are of less interest to the community. To establish the feasibility of  $GPT_c$  driven synthesis and confirmation of new superconducting material, we narrowed the candidate pool using pragmatic criteria. To avoid the use of a dilution refrigerator and aim for a most likely success within the material space that Schoop lab can readily access, we required the following criteria:

1. We considered  $2\text{ K} < \text{Predicted } T_c < 10\text{ K}$ .
2. We required the classification probability  $> 0.75$ .
3. We removed compounds containing O, N, F (outside the expertise of the lab), Os, Be, Tl, As (because of toxicity), Mn, Gd (usually lead to magnetism), H (hard to characterize), and radioactive elements.
4. We only kept stoichiometric (undoped) compounds with up to three distinct elements, to make growing more straightforward.
5. We removed compounds whose chemical formula contains 10 or more of the same elements, since it would be hard to establish that the correct composition was indeed grown.

6. We removed compounds that have a large band gap ( $> 0.1$  eV), either according to density functional theory (as recorded in the Materials Project [49, 50]) or according to our automated literature search (see the next section). While such insulators could be interesting as potential SCs upon doping, our initial proof of concept quest focused on undoped SCs.
7. We removed compounds containing a known elemental SC whose predicted  $T_c$  is within 1 K of the elemental SC’s  $T_c$ , since these could be mistaken for elemental SCs with impurities.

The resulting candidate list was forwarded to the Edison automated literature-precedence search agent to identify related compounds, known superconductors not represented in 3DSC, or materials with no documented history of superconductivity (see the next section for details). After applying these filters, we obtained a list of 173 potentially new, practically synthesizable SCs.

### C. Literature search for known superconductivity

Since the SuperCon database is not exhaustive and dated, some of the SCs predicted by  $GPT_c$  had been already confirmed. We therefore conducted a comprehensive literature search to identify any precedent. For materials in the filtered prediction list, we queried for known  $T_c$  with the prompt: Is [FORMULA] a known superconductor? If so, what is the highest reported Tc and what is the paper source?. Here, [FORMULA] is replaced with the chemical formula of the material.

We used Edison Scientific’s Precedent search agent for literature search (<https://edisonscientific.gitbook.io/edison-cookbook/edison-client>). With this prompt, Precedent (1) retrieved publications from the literature that are relevant to the material, (2) perused articles using a large language model, and (3) synthesized a report detailing prior superconductivity research on the material. The agent ensures an exhaustive literature search, i.e., maximizes knowledge recall, by leveraging multiple search rounds. Each time, the agent gathers more focused search results and incorporates information from previous rounds. Based on the PaperQA2 framework of Skarlinski *et al.* [51], the agent is optimized to answer questions such as “Has anyone done X before?” The full pipeline is proprietary.

For all materials, the Precedent search agent created reports of search results, including the reported  $T_c$  and publication references, if any. Even when no experimental  $T_c$  was reported, the reports often cited closely related superconducting materials, electronic or magnetic phase information, and insulating properties. The summaries of the properties and sources we list in our database will be valuable to the community in evaluating our predictions.

### D. Synthesis and characterization of PtPb<sub>3</sub>Bi

To validate our model’s predictive power, we synthesized PtPb<sub>3</sub>Bi, which  $GPT_c$  predicts to have  $T_c$  of 2.93 K, with a confidence of 0.756. This was a pragmatic choice as both Pb and Bi form deep eutectics with Pt, offering a low-temperature route to grow large single-crystals for experimental verification of its superconducting properties. Remarkably, magnetometry shown in Fig. 5(c–d) of the main text establishes that PtPb<sub>3</sub>Bi indeed undergoes a type-II superconducting transition with  $T_c \approx 2.98$  K. The temperature dependence of our magnetic susceptibility shows that the demagnetized-corrected, field-cooled curve reaches a value of  $4\pi\chi_v \sim -1.06$ , suggesting a newly discovered, phase-pure superconductor.

#### 1. Materials and Synthesis

Samples of PtPb<sub>3</sub>Bi were synthesized using a self-flux method utilizing a Canfield crucible. In the bottom crucible, 7 at% Pt (powder, Sigma Aldrich, 99.995%), 69.75 at% Pb (shot, Alfa Aesar, 99.999%), and 23.25 at% Bi (pieces, Sigma Aldrich, 99.999%) were weighed out and combined, totaling 2g. The Canfield crucible setup was then placed in a quartz tube, flushed with Ar 3 times, and sealed under vacuum at 80 mTorr. The sealed quartz tube was then placed in an induction furnace, ramped to 500°C over 5 hours and held at 500°C for 48 hours to ensure homogenization of precursors. The furnace was subsequently slowly cooled to 300°C at a rate of 4K/hour, and held at 300°C for 48 hours before centrifuging. The sample resulted in an ingot consisting of large metallic crystals, within a Pb matrix. Crystals used in measurements were then mechanically separated from the Pb matrix.

## 2. Single Crystal X-ray diffraction

Single crystal X-ray diffraction measurements were performed at room temperature using a Rigaku XtaLAB Synergy-S/i diffractometer equipped with a Mo  $K_{\alpha 1}$  ( $\lambda = 0.71073 \text{ \AA}$ ), micro-focus sealed-tube X-ray source and a graphite monochromator. Integration was carried out using CrysAlis<sup>Pro</sup> software, with numerical absorption correction based on gaussian integration over a multifaceted crystal model. Full structural refinements on  $F^2$  were performed in JANA2020.

Unit cell finding finds the previously reported cell as a tetragonal cell with  $a = 11.4557(8) \text{ \AA}$  and  $c = 4.0836(3) \text{ \AA}$ . Refinement proceeds smoothly in the previously reported space group of  $tP4_2/mnm$ .

Crystallographic refinement information, atomic coordinates, anisotropic parameters, and distances are given in Tables S4-S7.

TABLE S4. Crystallographic Information for PtPb<sub>3</sub>Bi.

Refined Composition	PtPb <sub>3</sub> Bi
Crystal Dimension (mm)	0.033 × 0.036 × 0.134
Radiation Source, $\lambda$ ( $\text{\AA}$ )	Mo $K_{\alpha}$ , 0.71073
Absorption Correction	Gaussian
Data Collection Temperature (K)	293.15(10)
Space Group	$P 4_2/mnm$
$a$ ( $\text{\AA}$ )	11.4557(8)
$c$ ( $\text{\AA}$ )	4.0836(3)
Cell Volume ( $\text{\AA}^3$ )	535.90(6)
Absorption Coefficient ( $\text{mm}^{-1}$ )	152.65
$\theta_{\min}$ , $\theta_{\max}$ (deg)	2.51, 39.97
Refinement Method	$F^2$
$R_{int}(I>3\sigma)$ , all	30.22, 31.85
Number of Parameters	19
Unique Reflections ( $I>3\sigma$ , all)	1007, 543
$R(I>3\sigma)$ , $R_w(I>3\sigma)$	5.19, 9.46
$R(\text{all})$ , $R_w(\text{all})$	11.55, 10.16
$S(I>3\sigma)$ , $S(\text{all})$	2.0887, 1.6347
$\Delta\rho_{\max}$ , $\Delta\rho_{\min}$ ( $e \text{ \AA}^{-3}$ )	8.77, -7.87

TABLE S5. Refined atomic coordinates for PtPb<sub>3</sub>Bi.

Site	Wyckoff Position	x	y	z	Occupancy
Pt1	4f	0.58675(6)	0.58675(6)	0	1
Pb1	4f	0.39768(6)	0.60232(6)	1/2	1
Pb2	8i	0.50243(7)	0.82996(7)	0	1
Bi1	4g	0.70728(6)	0.70728(6)	-1/2	1

TABLE S6. Refined anisotropic displacement parameters for PtPb<sub>3</sub>Bi.

Site	$U_{11}$	$U_{22}$	$U_{33}$	$U_{12}$	$U_{13}$	$U_{23}$
Pt1	0.0226(3)	0.0226(3)	0.0222(5)	-0.0030(3)	0	0
Pb1	0.0217(3)	0.0217(3)	0.0213(5)	0.0010(3)	0	0
Pb2	0.0263(3)	0.0235(3)	0.0332(4)	0.0015(2)	0	0
Bi1	0.0209(3)	0.0209(3)	0.0218(5)	-0.0005(3)	0	0

TABLE S7. Selected interatomic distances for PtPb<sub>3</sub>Bi.

Site	Neighbor	Multiplicity	Distance (Å)
Pt1	Pt1	1	2.8109(10)
Pt1	Pb1	4	2.9819(8)
Pt1	Pb2	1	2.9488(11)
Pt1	Bi1	2	2.8252(7)
Pb1	Pb1	1	3.3153(10)
Pb1	Pb2	4	3.5227(9)
Pb1	Bi1	2	3.7449(11)
Pb1	Bi1	2	3.6992(8)
Pb2	Pb2	4	3.4292(9)
Bi1	Pb2	2	3.4080(11)
Bi1	Pb2	2	3.4133(9)

### 3. Energy Dispersive X-ray Spectroscopy

Crystals of PtPb<sub>3</sub>Bi that were mechanically removed from an ingot were characterized using energy-dispersive x-ray spectroscopy in a Quanta environmental scanning electron microscope equipped with an Oxford EDX detector. Compositional analysis and sample homogeneity is shown in Fig. S9.

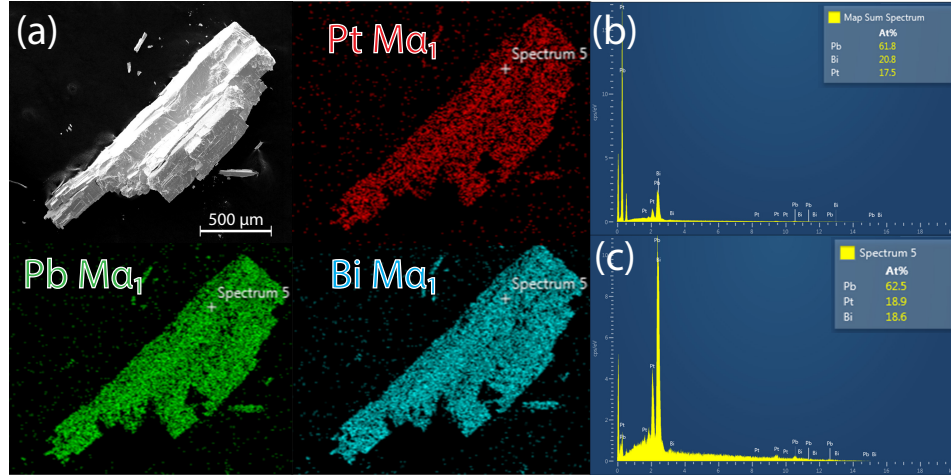


FIG. S9. **Chemical composition analysis of PtPb<sub>3</sub>Bi via EDX** (a) Elemental mapping of constituent elements in PtPb<sub>3</sub>Bi, showing homogeneous signal throughout the mapped crystal. (b) Map-sum and (c) Point spectra of the picked crystal, confirming the stoichiometry of the sample as PtPb<sub>3</sub>Bi.

### 4. Superconductivity Characterization

Data for DC magnetic susceptibility measurements utilized a Quantum Design Magnetic Properties Measurement system. A single crystal, shown at the inset of Fig. S10, was mounted on a quartz holder with GE varnish. The sample was mounted with the *c*-axis aligned parallel to the applied magnetic field to minimize demagnetization effects. Data points for M-T sweeps were taken at  $\sim 0.005$  K intervals, with field-cooled data taken with an applied field of  $\sim 5$  Oe.

The sample volume was determined by the total mass of the sample, 3.04 mg, and the nominal density of the sample, 12.712 g/cm<sup>3</sup>. The volume-weighted measured total moment was then deduced by dividing the total magnetic moment by this volume.

We then corrected the internal field due to demagnetization factors

$$H_{\text{int}} = H_{\text{app}} - 4\pi NM, \quad (\text{S29})$$

where  $H_{\text{int}}$  is the internal magnetic field,  $H_{\text{app}}$  is the apparent magnetic field,  $N$  is the demagnetization factor that is geometrically dependent, and  $M$  is the magnetization of the sample. We estimate our crystal as a rectangular prism geometry with the  $c$ -axis parallel to the applied magnetic field [52, 53], in this case

$$N \approx \frac{4AB}{4AB + 3C(A + B)}, \quad (\text{S30})$$

where  $A$  and  $B$  are lengths of the crystal perpendicular to the applied magnetic field, and  $C$  is the length of the crystal parallel to the crystal field. For the demagnetization factor we note that our measured crystal, shown in Fig. S10 is not a perfect rectangular prism. For our calculation of  $N$ , we estimate the values of  $A = 0.35$  mm,  $B = 0.37$  mm and  $C = 1.74$  mm, where the length of  $C$  is estimated for a rectangular prism that conserves the total volume of the sample. This results in a demagnetization factor of  $N \approx 0.1211$ . This estimation of  $C$  should slightly overestimate the true value of  $N$ . The slight overshooting of the expected phase pure superconducting value (-1) can be attributed to the extra diamagnetic signal of the GE varnish and quartz holder.

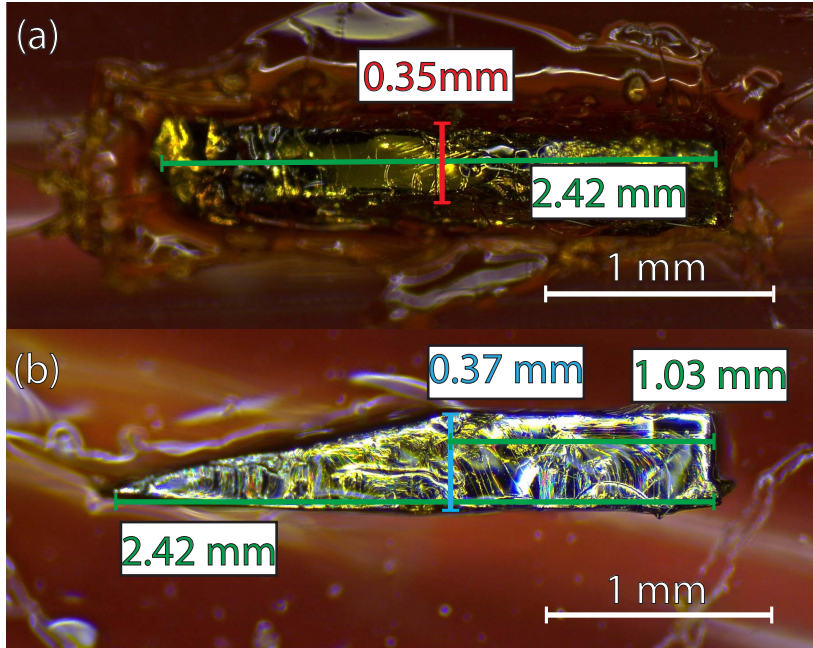


FIG. S10. **Geometry of crystal measured in magnetic susceptibility measurements** (a) Crystal measurements of  $A$  (red) and  $C$  (green). (b) Crystal measurements of  $B$  (blue) and  $C$  (green).

In Fig. S11, we show the magnetic susceptibility of both the uncorrected and corrected M-T and M-H runs.

Alternating current electronic transport measurements were performed using a Quantum Design Physical Property Measurement System. Gold wires were connected in a four probe geometry using conducting silver paste (Dupont 4929N) to the same crystal measured in our magnetization data.

Field dependent  $\rho$ - $T$  curves were taken under different applied fields at intervals of 500 Oe (Fig. S12(a)). All fields show a drop to 0 resistivity at low temperatures. At zero applied field, the resistivity drops by 50% at 3.009 K, further confirming the bulk superconducting transition shown in our  $M - T$  curves. Further, the transition width, which we define as the change in temperature between the 90% and 10% drop in resistivity, is only 0.111 K, indicating that our sample is of high crystalline quality. Upon increasing the applied field, the transition temperature for PtPb<sub>3</sub>Bi decreases and the transition width increases, as expected for a type-II superconductor.

The isotherms of  $\rho - \mu_0 H$  (Fig. S12(b)) also display expected behavior for superconductivity, where increasing temperature reduces the upper critical field towards the normal state. Utilizing the data from both  $\rho$ - $T$  and  $\rho - \mu_0 H$  experiments, we then plot a phase diagram for our upper critical field (Fig. S12(c)). A simple Werthamer-Helfand-Hohenberg (WHH) fit to this data suggests an estimate to the upper critical field as  $\mu_0 H_{c2}(0) = 0.6672$  T. This upper critical field falls far below the Pauli limit,  $H_P \approx 1.86 \times 3.0 \approx 5.6$  T, suggesting an orbital-pair breaking mechanism.

Temperature- and frequency-dependent  $I - V$  curves are shown in Fig. S12(d) and (e), both displaying expected behavior for superconductivity. At 1.8 K an AC current frequency of 97.6 Hz has the highest measured critical current

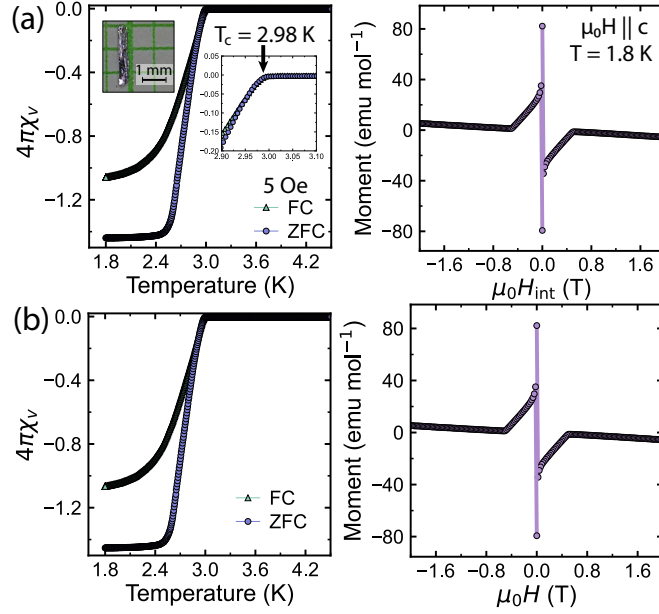


FIG. S11. **Demagnetization correction for M-T and M-H sweeps** (a) M-T and M-H sweeps of PtPb<sub>3</sub>Bi with applied demagnetization correction  $N = 0.1211$ . (b) M-T and M-H sweeps of PtPb<sub>3</sub>Bi without any demagnetization correction.

of  $\sim 33$  mA. Lower AC frequencies result in lower critical currents, consistent with the relaxation of vortices only seen in type-II superconductors.

It is interesting to note that newly confirmed superconductor PtPb<sub>3</sub>Bi shares key 2nd-order graphlet features we have identified, electron affinity differences, and interatomic distances, with PtPb<sub>4</sub> ( $T_c \sim 2.75$  K) that has been recently characterized [54–56]. The two materials are markedly different in their structures, as shown in Fig. S13. Specifically, PtPb<sub>4</sub> hosts edge-sharing [PtPb<sub>8</sub>] square antiprisms in quasi-two-dimensional layers, while PtPb<sub>3</sub>Bi hosts face-sharing dimerized [Pt<sub>2</sub>Pb<sub>8</sub>Bi<sub>4</sub>] bicapped trigonal prismatic units, stacked along the *c*-axis forming a quasi-one-dimensional structure type. Critically, PtPb<sub>3</sub>Bi forms in its own unique structure type with no other reported variants to the best of our knowledge. Hence, the prediction of superconductivity in PtPb<sub>3</sub>Bi would have escaped any structure-focused approach, including a focus on structural motifs. On the other hand, the GPT<sub>c</sub>'s success in correctly predicting  $T_c$  for PtPb<sub>3</sub>Bi to be close to that of PtPb<sub>4</sub> demonstrates the power of our four features in Fig 4(a).

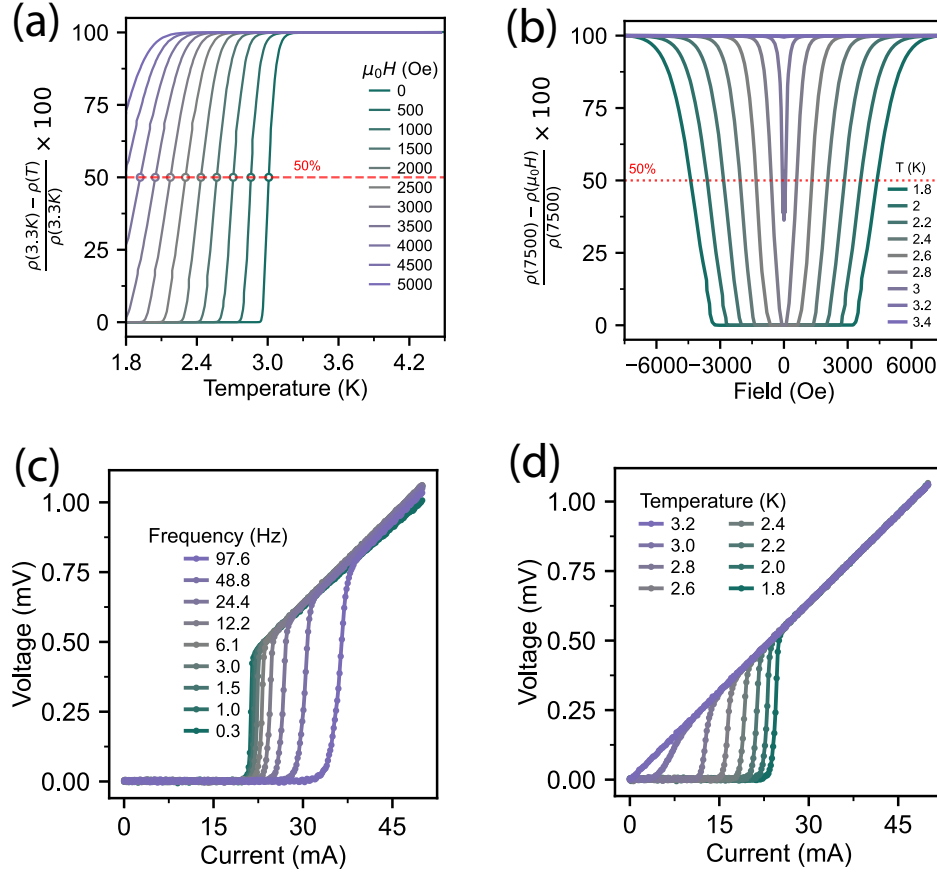


FIG. S12. **Electronic transport data for PtPb<sub>3</sub>Bi.** (a) Temperature dependent resistivity at different applied field confirm a bulk superconductivity drop at 3.0 K, consistent with our magnetization data. (b) Field dependent resistivity (magnetoresistivity) at different temperatures. (d) Temperature- and (e) frequency-dependent  $I - V$  curves consistent with a type-II superconducting transition.

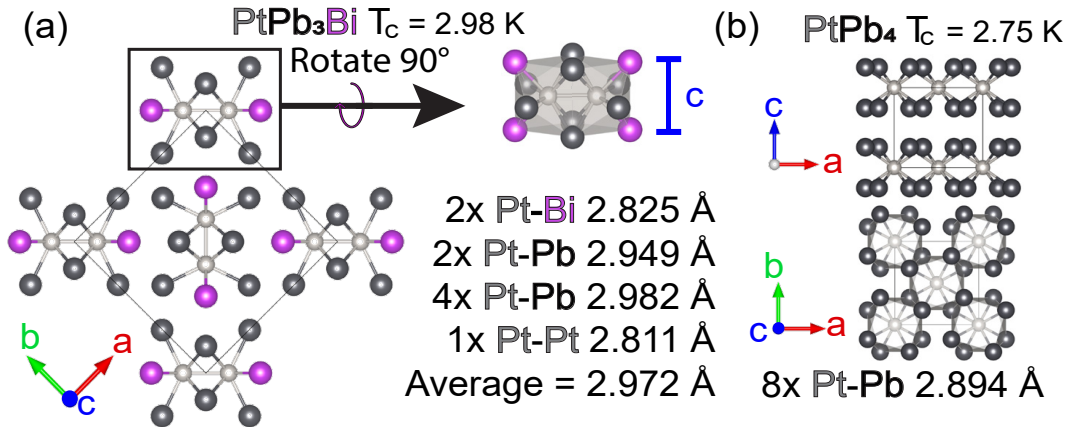


FIG. S13. **Structural comparison of PtPb<sub>3</sub>Bi and PtPb<sub>4</sub>.** (a) PtPb<sub>3</sub>Bi, a quasi-one-dimensional structure type with no other reported structural variants. The quasi-one-dimensional units are built up of dimerized bi-capped trigonal prismatic units, stacked along the c-axis. (b) PtPb<sub>4</sub>, built up of edge-sharing square antiprisms in a quasi-two-dimensional structure type. Recent characterization has classified it as a superconductor with  $T_c \sim 2.75$  K [54–56].